PACIFIC EARTHQUAKE ENGINEERING
RESEARCH CENTER

Effect of Damping Mechanisms on the Response of Seismically Isolated Structures

Nicos Makris
Shih-Po Chang
University of California, Berkeley

PEER 1998/06
NOV. 1998

Effect of Damping Mechanisms on the Response of Seismically Isolated Structures

Nicos Makris

and

Shih-Po Chang
Department of Civil and Environmental Engineering
University of California, Berkeley

PEER Report 1998/06
Pacific Earthquake Engineering Research Center
College of Engineering
University of California, Berkeley

November 1998

ABSTRACT

In this report the efficiency of various dissipative mechanisms to protect structures from pulse-type and near-source ground motions is examined. It is first shown that under such motions the concept of equivalent linear damping has limited meaning since the transient response of a structure is more sensitive to the nature of the dissipation mechanism, rather than to the amount of energy dissipated per cycle. Subsequently, physically realizable cycloidal pulses are introduced, and their resemblance to recorded near-source ground motions is illustrated. The study uncovers the coherent component of some near-source acceleration records, and the shaking potential of these records is examined. It is found that the response of structures with relatively low isolation periods is substantially affected by the high frequency fluctuations that override the long duration pulse. Therefore, the concept of seismic isolation is beneficial even for motions that contain a long duration pulse which generates most of the unusually large recorded displacements and velocities of near-source events. Dissipation forces of the plastic (friction) type are very efficient in reducing displacement demands although occasionally they are responsible for substantial base shears. It is found that the benefits of hysteretic dissipation are nearly indifferent to the level of the yield displacement of the hysteretic mechanism and that they depend primarily on the level of the plastic (friction) force. Supplemental viscous damping to hysteretic mechanisms further reduces displacements in the superstructure. The study concludes that a combination of relatively low friction and viscous forces is most attractive since base displacements are substantially reduced without appreciably increasing base shear and superstructure accelerations.

TABLE OF CONTENTS

LIST OF FIGURES

ACKNOWLEDGEMENTS

Partial financial support for this study was provided by the National Science Foundation under Grant CMS-9696241 and the California Department of Transportation under Grant RTA-59A169. The valuable comments offered by Dr. Tim Delis are appreciated.

CHAPTER 1

INTRODUCTION

The dynamic response of a structure depends on its mechanical characteristics and the nature of the induced excitation. Mechanical properties which are efficient to mitigate the structure's response when subjected to certain inputs might have an undesirable effect during other inputs. Ground motions generated from earthquakes differ from one another in magnitude, source, characteristics, distance and direction from the rupture location and local soil conditions. The ability of a structure to dissipate energy is central to controlling displacement demands, and various energy dissipation mechanisms have been proposed to enhance structural response (ATC, 1993). These energy dissipation mechanisms can be of various types such as viscous, rigid-plastic, elastoplastic, viscoplastic, or combination of thereof.

Under seismic excitations that have relatively long durations, a structure undergoes several cycles during the forced vibration part of the response; therefore, its response depends more on the amount of energy that is dissipated during each cycle (area under the force-displacement loop) than on the nature of the dissipative force that develops (viscous, friction, elastoplastic or viscoplastic). Because of this, the dissipation properties of structures have been traditionally averaged over a cycle of motion and expressed in term of dimensionless ratios which originate from the linear theory of structural dynamics (Clough and Penzien 1993, Chopra 1995).

During the last two decades, an ever increasing database of recorded ground motions have demonstrated that the kinematic characteristics of the ground motion near the faults of major earthquakes contain large displacement pulses from 0.5 m to more than 1.5 m with peak velocities of 0.5 m/sec or higher. In some cases, the coherent pulse is distinguishable not only in the displacement and velocity histories, but also in the acceleration history, which happens to be a rather smooth signal. In other cases, acceleration histories recorded near the source contain high-frequency spikes and resemble the traditional random-like signal; however, their velocity and displacement histories uncover a coherent long-period pulse with some overriding high-frequency fluctuations (Anderson et al. 1986, Campillo et al. 1989, Iwan and Chen 1994).

The challenge in providing seismic protection from such motions is the selection of mechanical properties that will improve the response of a structure subjected to a high-frequency spike and a low-frequency, low-acceleration pulse. Previous studies (Anderson and Bertero 1986, Hall et al. 1995, Iwan 1997) indicated that what makes near-source ground motions particularly destructive to some structures is not their peak ground acceleration but their long duration pulse, which represents the incremental velocity that the above-ground mass has to reach. These indications challenged the concept of seismic isolation. This report addresses this challenge in a systematic way, showing that seismic isolation is an effective protection strategy against near-source ground motions provided that the appropriate energy dissipation mechanism is provided.

In this study the effect of various dissipation mechanisms in reducing the response of seismically isolated structures subjected to near-source ground motions is examined in detail. It is first shown through a comprehensive study that during pulse-type ground motions the concept of equivalent linear damping is no longer valid because the response is strongly transient. The response of the structure is much more sensitive to the nature of the dissipation mechanism, than to the amount of energy dissipated per cycle. Accordingly, damping ratio quantities used in design, such as the effective damping coefficient, β_{eff}, should be used with caution. Subsequently, selected near-source ground motions are presented, and their resemblance to physically realizable cycloidal pulses is shown. A type-A cycloidal pulse approximates a forward motion; a type-B cycloid pulse approximates a forward-and-back motion; whereas, a type-C_n pulse approximates a recorded motion that exhibits n main pulses in its displacement history. The velocity histories of all type-A, type-B and type-C_n pulses are differentiable signals that result in finite acceleration values.

While the proposed cycloidal pulses capture many of the kinematic characteristics of the displacement and velocity histories of recorded near-source ground motions, in many cases the resulting accelerations are poor predictions of the recorded histories. This is because in many near-source ground motions there are high frequency fluctuations that override the long duration pulse. It is shown that the response of structures with relatively low isolation periods is affected significantly by these high frequency fluctuations, indicating that the concept of seismic protection by lengthening the isolation period is beneficial when the appropriate type of energy dissipation is provided. The benefits of rigid-plastic or elastic-plastic behavior are nearly indifferent to

the level of the yield displacement and depend primarily on the level of the plastic (friction) force. The report concludes that a combination of relatively low values of plastic (friction) and viscous damping results in an attractive design since displacements are substantially reduced without appreciably increasing base shear and superstructure accelerations.

CHAPTER 2

MODAL DAMPING RATIO AND EFFECTIVE DAMPING COEFFICIENT

In order to represent the ability of a structure or a structural component to dissipate energy various dimensionless quantities have been proposed to express damping. This section reviews the definitions and relations of the two most widely used ratios, that of the modal damping ratio, ξ_i, and that of the effective damping coefficient, β_{eff}.

For a 1-DOF linear oscillator with mass, m, stiffness, $K = m\omega_0^2$, and viscous damping, C, the viscous damping ratio is defined as $\xi = C/(2m\omega_0)$. Since for a 1-DOF there is only one mode, the first modal damping, ξ_1, = ξ. Clearly, the modal damping (viscous damping ratio) has meaning only when the structural system has finite inertial mass ($m \neq 0$).

During a steady-state harmonic motion with amplitude, U_0, and frequency, Ω, the damping constant, C, is related to the energy dissipated per cycle, W_D,with

$$C = 2\xi m\omega_0 = \frac{W_D}{\pi\Omega U_0^2} \tag{1}$$

where W_D is the area under the steady-state force-displacement loop. Recognizing that the maximum strain energy stored in the oscillation during this motion is $E_s = \frac{1}{2}m\omega_0^2 U_0^2$, the damping coefficient, ξ, is

$$\xi = \frac{1}{4\pi}\frac{\omega_0}{\Omega}\frac{W_D}{E_s}\ . \tag{2}$$

When the frequency of vibration of the 1-DOF system happens to be the natural frequency of the oscillator (resonance), then the modal damping, ξ, = $W_D/(4\pi E_s)$, which is the familiar expression presented in most books of structural and soil dynamics (Chopra 1995, Kramer 1996).

With the development of seismic protection systems and energy dissipation devices, structural engineers faced the need to quantify the energy dissipation capabilities of isolation compo-

nents with virtually no inertial mass (during component testing, the inertia forces recorded by the load cell are very small compared to the forces originating from elasticity and dissipation). The most popular way to quantify energy dissipation of a protective device is to impose a cyclic displacement $U(t) = U_0 \sin \Omega t$ on the device and measure the resulting force that develops. During such tests the energy dissipated per cycle is the area under the force displacement loop and the effective damping coefficient, β_{eff}, of the protective device is defined as

$$\beta_{eff} = \frac{1}{2\pi} \frac{W_D}{K_I U_0^2}, \tag{3}$$

where K_I is the effective stiffness of the isolation device.

Consider now the 1-DOF system shown in Figure 1 (top), which consists of a rigid block with mass *m* supported on an isolation system with effective stiffness $K_I = m\omega_I^2$. For this structural system, the combination of (2) and (3) gives

$$\xi = \xi_1 = \frac{\omega_I}{\Omega} \beta_{eff}, \tag{4}$$

where $\omega_I = \sqrt{K_I / m}$ and Ω is the frequency at which the superstructure oscillates. Equation (4) relates the modal damping of a structural system with finite mass to the effective damping coefficient, β_{eff}, of an isolation system with virtually no mass. On many occasions during earthquake shaking the superstructure oscillates near its natural frequency ($\Omega \approx \omega_I$), and, because of equation (4), it has become a practice to assume $\xi \approx \beta_{eff}$. However, as will be shown in this report, despite the fact that structures oscillates with their natural frequencies under pulse-type motions, $\xi \neq \beta_{eff}$.

Consider now the 2-DOF base isolated structure shown in Figure 1 (bottom). The isolation frequency of the structure is $\omega_I = \sqrt{K_I / (m_b + m)}$, where K_I is again the effective stiffness of the isolation system. The natural frequency of the fixed base superstructure is $\omega_s = \sqrt{K_s / m}$. Furthermore, the isolation damping is defined as $C_I = 2\xi_I (m_b + m)\omega_I$ and the superstructure damping is defined as $C_s = 2\xi_s m \omega_s$. The 2-DOF structure shown in Figure 1 (bottom) has two modes, and the modal frequencies and modal damping ratios are given in the following by Kelly (1997):

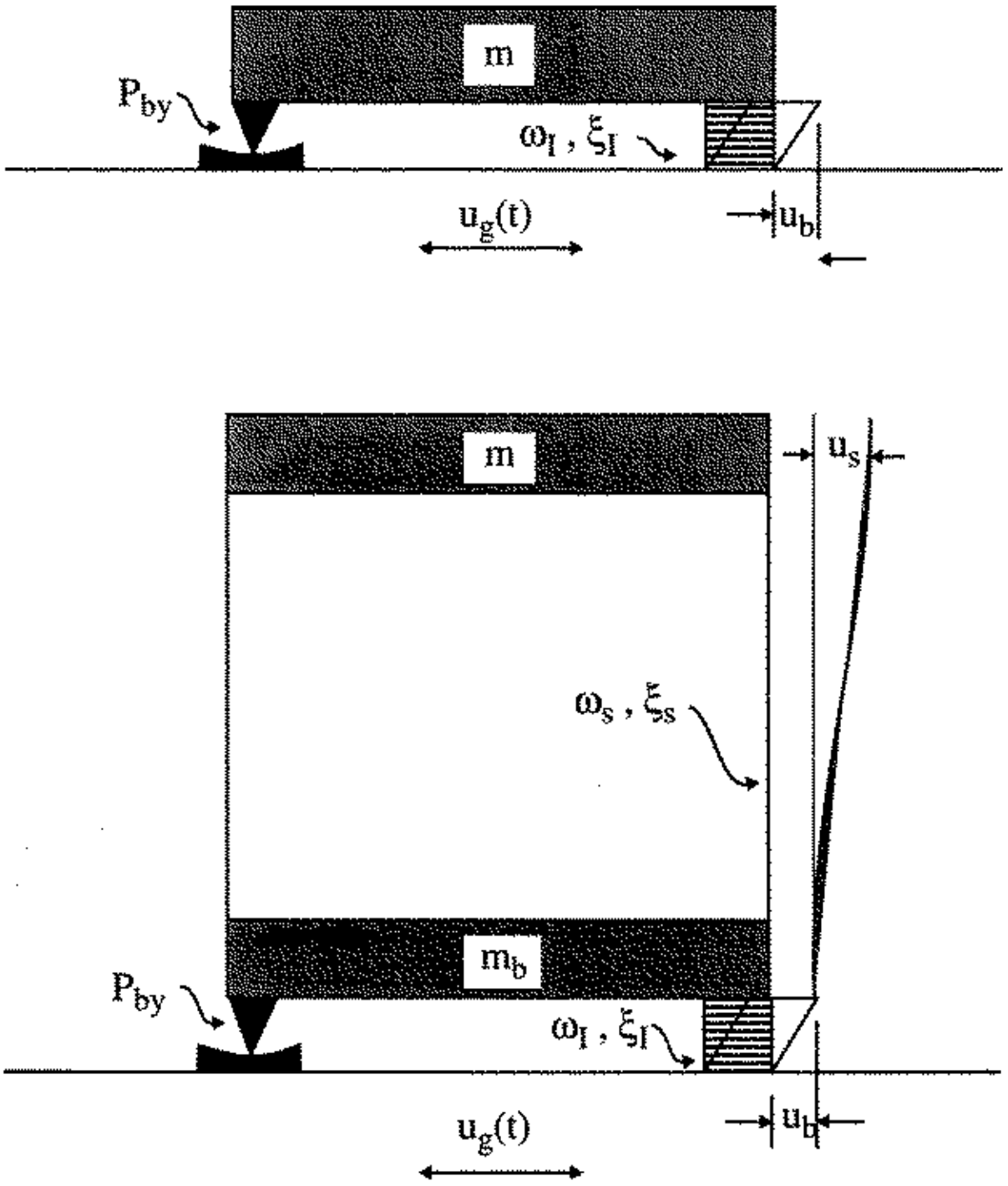

Figure 1: Schematic of an isolated rigid block (top) and of a two degree of freedom isolated structure (bottom).

$$\omega_1 = \omega_I \sqrt{1 - \gamma \frac{\omega_I^2}{\omega_s^2}}, \qquad \xi_1 = \xi_I \left(1 - \frac{3}{2} \gamma \frac{\omega_I^2}{\omega_s^2} \right), \tag{5}$$

$$\omega_2 = \frac{\omega_s}{\sqrt{1-\gamma}} \sqrt{1 + \gamma \frac{\omega_I^2}{\omega_s^2}}, \qquad \xi_2 = \frac{1}{\sqrt{1-\gamma}} \left(\xi_s + \xi_I \gamma \frac{\omega_I}{\omega_s} \right) \left(1 - \frac{1}{2} \gamma \frac{\omega_I^2}{\omega_s^2} \right), \tag{6}$$

where $\gamma = m/(m + m_b)$. Because of the presence of the isolation system, the participation of the first mode is dominant, and the 2-DOF structure will primarily oscillate along its first mode. Accordingly,

$$\xi_1 = \frac{1}{4\pi} \frac{W_D(\omega_1)}{E_s} = \beta_{eff}(\omega_1) \approx \xi_I \, . \tag{7}$$

Since the effective damping coefficient of most isolation systems is nearly frequency independent, it has now become a practice to assume that $\xi_1 = \xi_I = \beta_{eff}$. This relation also is no longer valid during pulse-type excitations.

CHAPTER 3

CLOSED FORM APPROXIMATION OF NEAR-SOURCE GROUND MOTIONS

Figure 2 (left) shows the East-West components of the acceleration, velocity and displacement histories of the September 19th, 1985 Michoacan earthquake recorded at the Caleta de Campos station (Anderson et al. 1986). The motion resulted in a forward displacement of the order of 0.4 m. The coherent long duration pulse responsible for most of this displacement can also be distinguished in the velocity history, whereas the acceleration history is crowded with high frequency spikes. Figure 2 (right) plots the acceleration, velocity and displacement histories of a type-A cycloidal pulse given by the following (Jacobsen and Ayre 1958, Makris 1997):

$$\ddot{u}_g(t) = \omega_p \frac{v_p}{2} \sin(\omega_p t),\ 0 \le t \le T_p, \tag{8}$$

$$\dot{u}_g(t) = \frac{v_p}{2} - \frac{v_p}{2} \cos(\omega_p t),\ 0 \le t \le T_p, \tag{9}$$

$$u_g(t) = \frac{v_p}{2} t - \frac{v_p}{2\omega_p} \sin(\omega_p t),\ 0 \le t \le T_p. \tag{10}$$

In constructing Figure 2 (right), the values of T_p = 5.0 s and v_p = 0.16 m/s were used. These are approximations of the duration and velocity amplitude of the main pulse. Figure 2 indicates that a simple one-sine pulse can capture some of the kinematic characteristics of the motion recorded at the Caleta de Campos station. On the other hand, the resulting acceleration amplitude, $a_p = \omega_p v_p / 2 \approx 0.01g$, is one order of magnitude smaller than the recorded peak ground acceleration.

Another example of a recorded ground motion that resulted in a forward pulse is the fault parallel motion recorded at the Lucerne Valley station during the June 18th, 1992 Landers earthquake, which is shown in Figure 3 (left). Although the displacement history results in a clean forward pulse, the acceleration history is crowded with high-frequency spikes that reach 0.75 g. On the right of Figure 3, the results of equations (8) to (10) are shown for the values of T_p = 7.0 s and v_p = 0.5 m/s, which are approximations of the pulse period and the pulse velocity amplitude

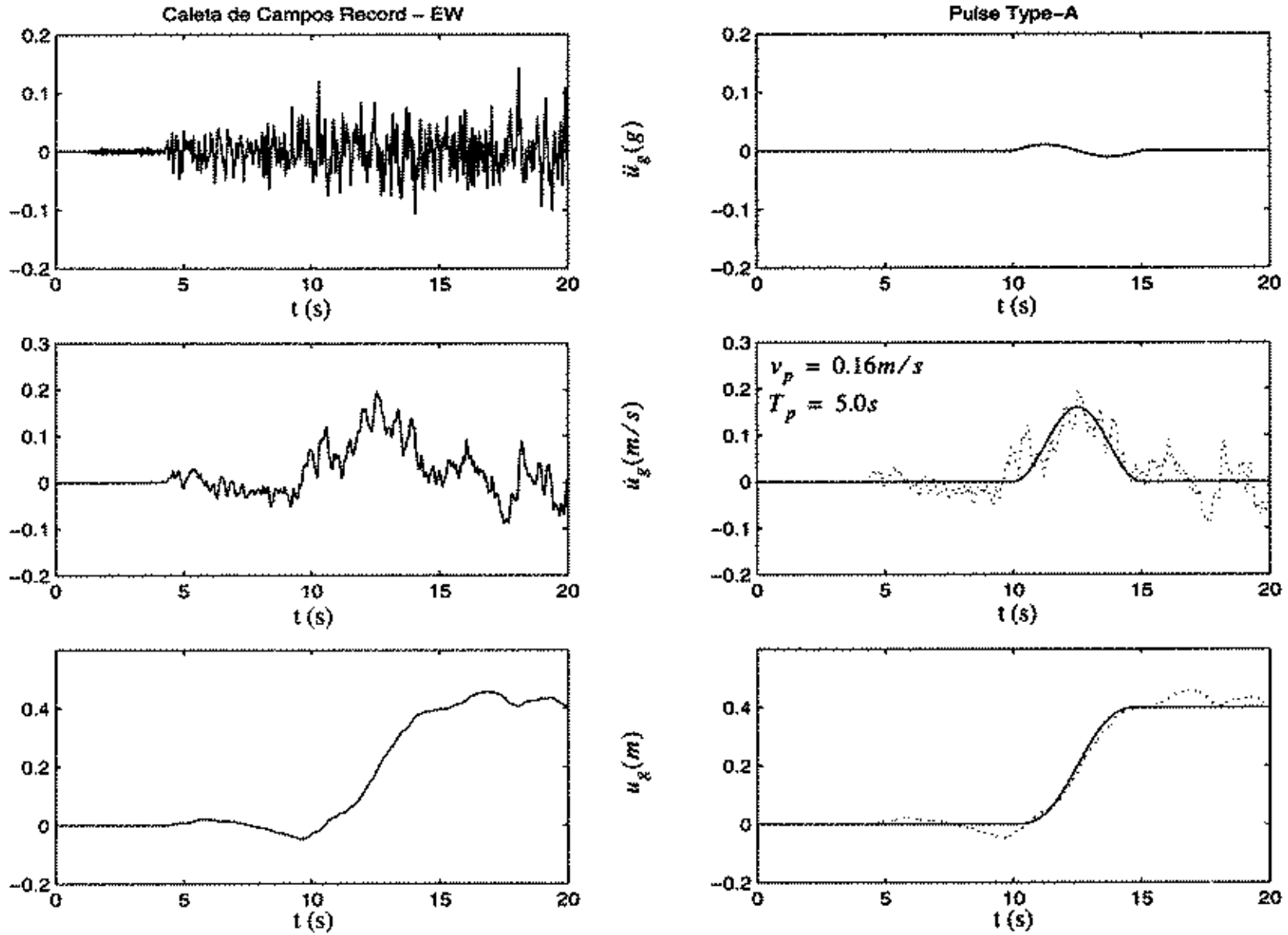

Figure 2: Fault normal components of the acceleration, velocity and displacement time histories recorded at the Caleta de Campos station during the September 19th, 1985 Michoacan, earthquake (left), and a cycloidal type-A pulse (right).

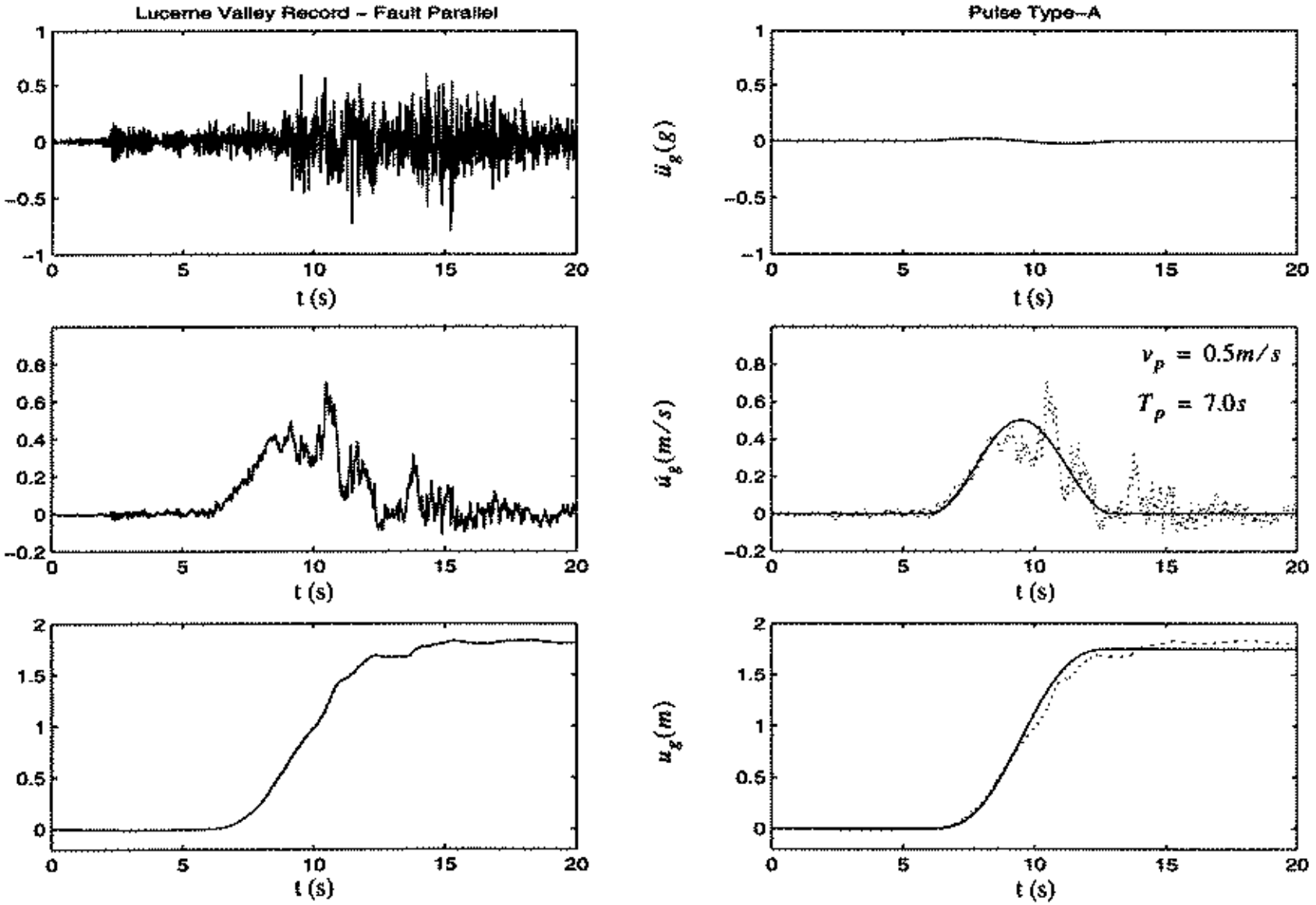

Figure 3: Fault parallel components of the acceleration, velocity and displacement time histories recorded at the Lucerne Valley station during the June 28th, 1992 Landers, California earthquake (left), and a cycloidal type-A pulse (right).

of the recorded motion. Again, while the resulting displacement history is in very good agreement with the record, the resulting acceleration amplitude, $a_p = \omega_p v_p / 2 \approx 0.045g$, is one order of magnitude smaller than the recorded peak ground acceleration.

Figure 4 (left) shows the acceleration, velocity and displacement histories of the fault-normal motions recorded at the El Centro Station Array #5 during the October 15th, 1979 Imperial Valley earthquake. This motion resulted in a forward-and-back pulse with a 3.2 sec duration. In this case, the coherent long period pulse is distinguishable not only in the displacement and velocity record, but also in the acceleration record. Figure 4 (right) plots the acceleration, velocity and displacement histories of a type-B cycloidal pulse given by Makris (1997).

$$\ddot{u}_g(t) = \omega_p v_p \cos(\omega_p t),\ 0 \le t \le T_p, \tag{11}$$

$$\dot{u}_g(t) = v_p \sin(\omega_p t),\ 0 \le t \le T_p, \tag{12}$$

$$u_g(t) = \frac{v_p}{\omega_p} - \frac{v_p}{\omega_p}\cos(\omega_p t),\ 0 \le t \le T_p. \tag{13}$$

In constructing Figure 4 (right), the values T_p = 3.2 sec and v_p = 0.7 m/s were used as approximate values of the pulse period and velocity amplitude of the recorded motions shown in Figure 4 (left).

Figure 5 (left) portrays the fault-normal components of the acceleration, velocity and displacement histories of the January 17th, 1994 Northridge earthquake recorded at the Rinaldi station. This motion resulted in a forward ground displacement that recovered partially. The velocity history has a large positive pulse and a smaller negative pulse that is responsible for the partial recovery of the ground displacement. Had the negative velocity pulse generated the same area as the positive velocity pulse, the ground displacement would have fully recovered. Accordingly, the fault normal component of the Rinaldi station record is in between a forward and a forward-and-back pulse. Figure 5 (center) shows the results of equations (8) to (10) by assuming a pulse duration T_p = 0.8 s and a velocity amplitude v_p = 1.75 m/s, which are approximations of the duration and velocity amplitude of the first main pulse shown in the record. Figure 5 (right) shows the results of equations (11) to (13) by considering a pulse duration T_p = 1.3 sec and a velocity

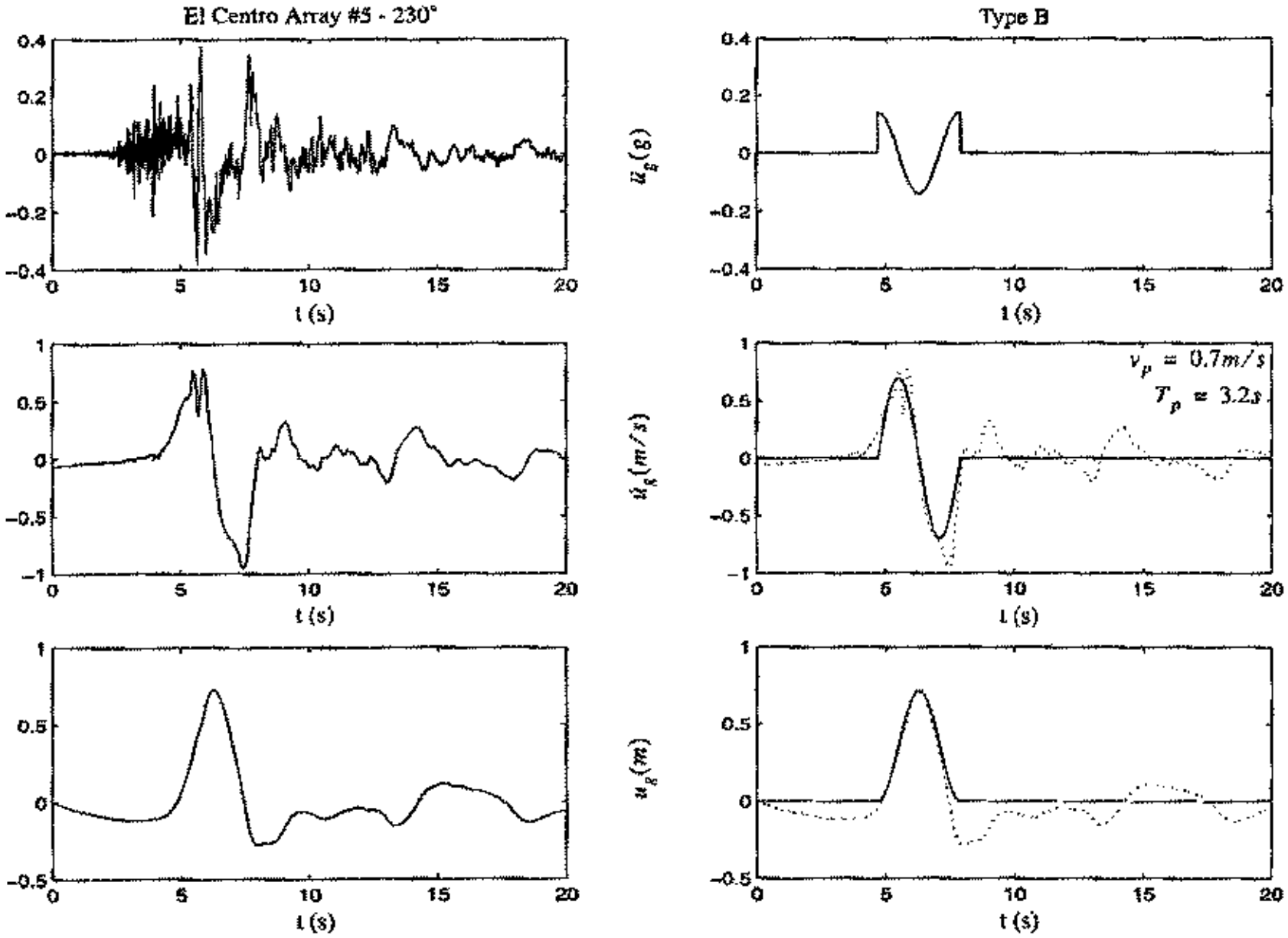

Figure 4: Fault normal components of the acceleration, velocity and displacement time histories recorded at the El Centro Array #5 station during the October 15th, 1979 Imperial Valley, California earthquake (left), and a cycloidal type-B pulse (right).

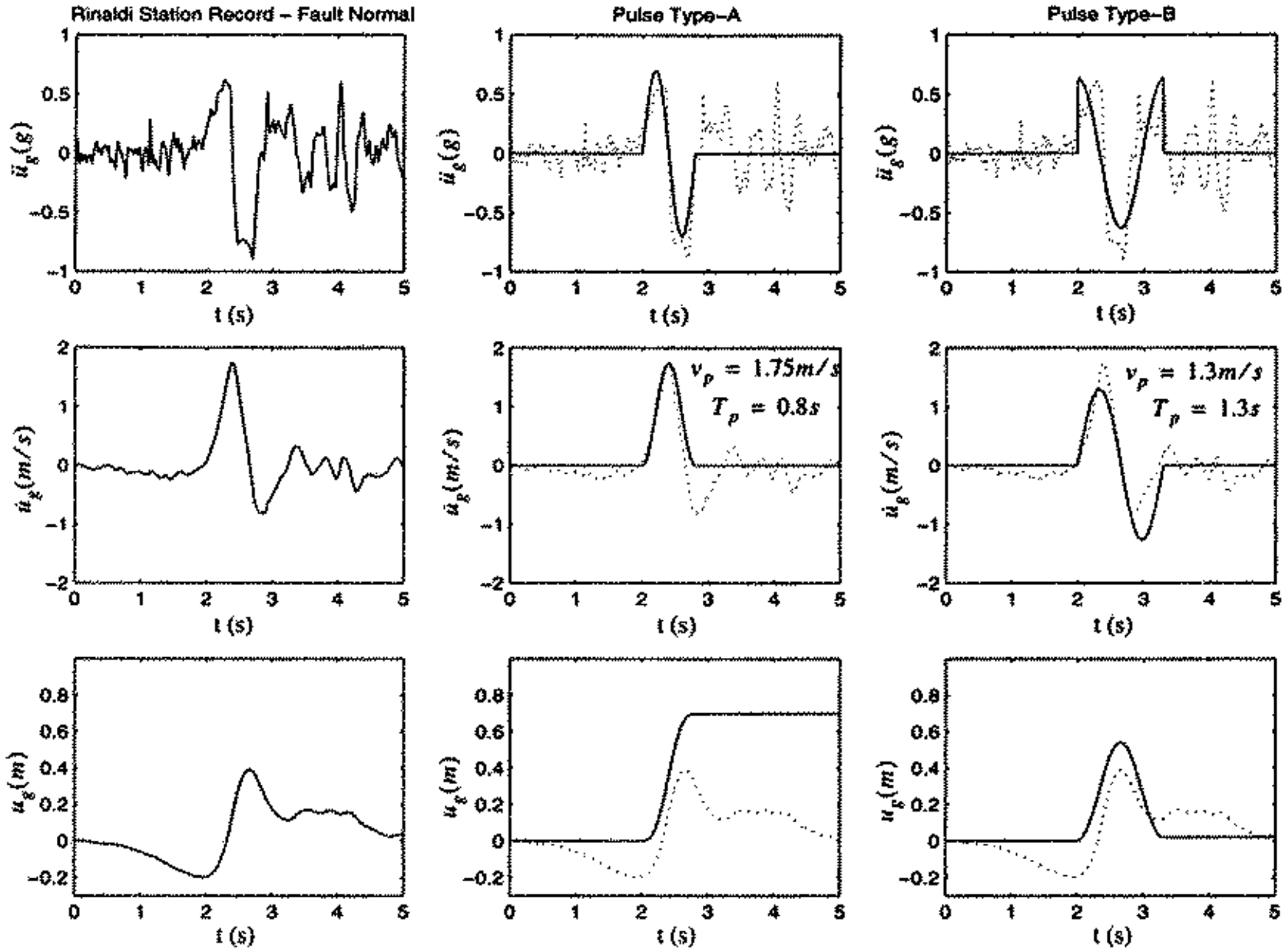

Figure 5: Fault normal components of the acceleration, velocity and displacement time histories recorded at the Rinaldi station during the January 17th, 1994 Northridge, California earthquake (left), a cycloidal type-A pulse (center) and a cycloidal type-B pulse (right).

amplitude v_p = 1.3 m/s. A similar situation prevails for the fault normal motion recorded at the Lucerne Valley station during the June 18th, 1992 Landers earthquake, which is shown in Figure 6 (left). Again, the velocity history has a large negative pulse that is followed by a smaller positive pulse. Had the second positive pulse generated the same area as the negative pulse, the ground displacement would have fully recovered. Figure 6 (center) shows the results of equations (8) to (10) by considering a pulse duration T_p = 3.0 sec. and a velocity amplitude v_p = 1.0 m/s, which are approximations of the duration and velocity amplitude of the first main pulse shown in the record. Figure 6 (right) shows the results of equations (11) to (13) by considering a pulse duration T_p = 5.0 sec and a velocity amplitude v_p = 1.0 m/s. Trends similar to those observed in Figure 3 are also present in Figure 6. Although the constructed displacement and velocity histories associated with either a type-A pulse or a type-B pulse capture distinct elements of the kinematics of the recorded motion, the resulting ground acceleration is an order of magnitude smaller than the peak recorded value.

Not all near source records are forward or forward-and-back pulses. Figure 7 (left) portrays the fault-normal component of the acceleration, velocity and displacement time histories recorded at the Sylmar station during the January 17th, 1994 Northridge earthquake. The ground displacement consists of two main long-period cycles, the first cycle being the largest, and the subsequent ones decaying. These long period pulses are also distinguishable in the ground velocity history where the amplitude of the positive pulses is larger than the amplitude of the negative pulses. Figure 8 (left) portrays the fault parallel components of the acceleration, velocity and displacement histories recorded at the Rinaldi station during the January 17th, 1994 Northridge earthquake. The ground displacement consists of two main long period cycles with subsequently decaying motions. Figure 9 (left) plots the fault-normal components of the acceleration, velocity and displacement time histories recorded at the Newhall station during the January 17th, 1994 Northridge earthquake. Near-fault ground motions, where the displacement history exhibits one or more long duration cycles, are approximated with type-C pulses. An n-cycle ground displacement is approximated with a type-C_n pulse, which is defined as

$$\ddot{u}_g(t) = \omega_p v_p \cos(\omega_p t + \varphi),\ 0 \le t \le \left(n + \frac{1}{2} - \frac{\varphi}{\pi}\right) T_p, \tag{14}$$

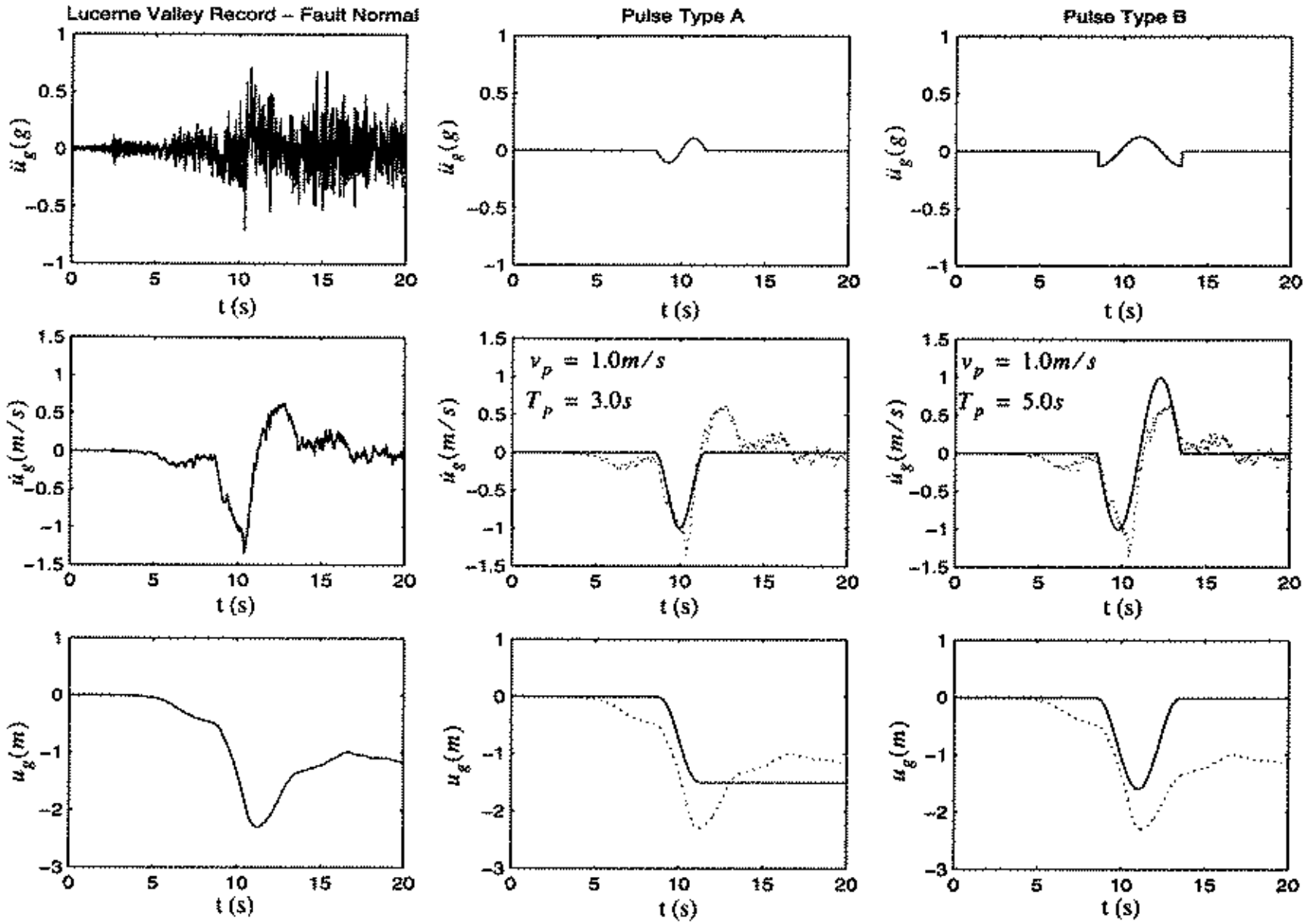

Figure 6: Fault normal components of the acceleration, velocity and displacement time histories recorded at the Lucerne Valley station during the June 28th, 1992 Landers, California earthquake (left), a cycloidal type-A pulse (center) and a cycloidal type-B pulse (right).

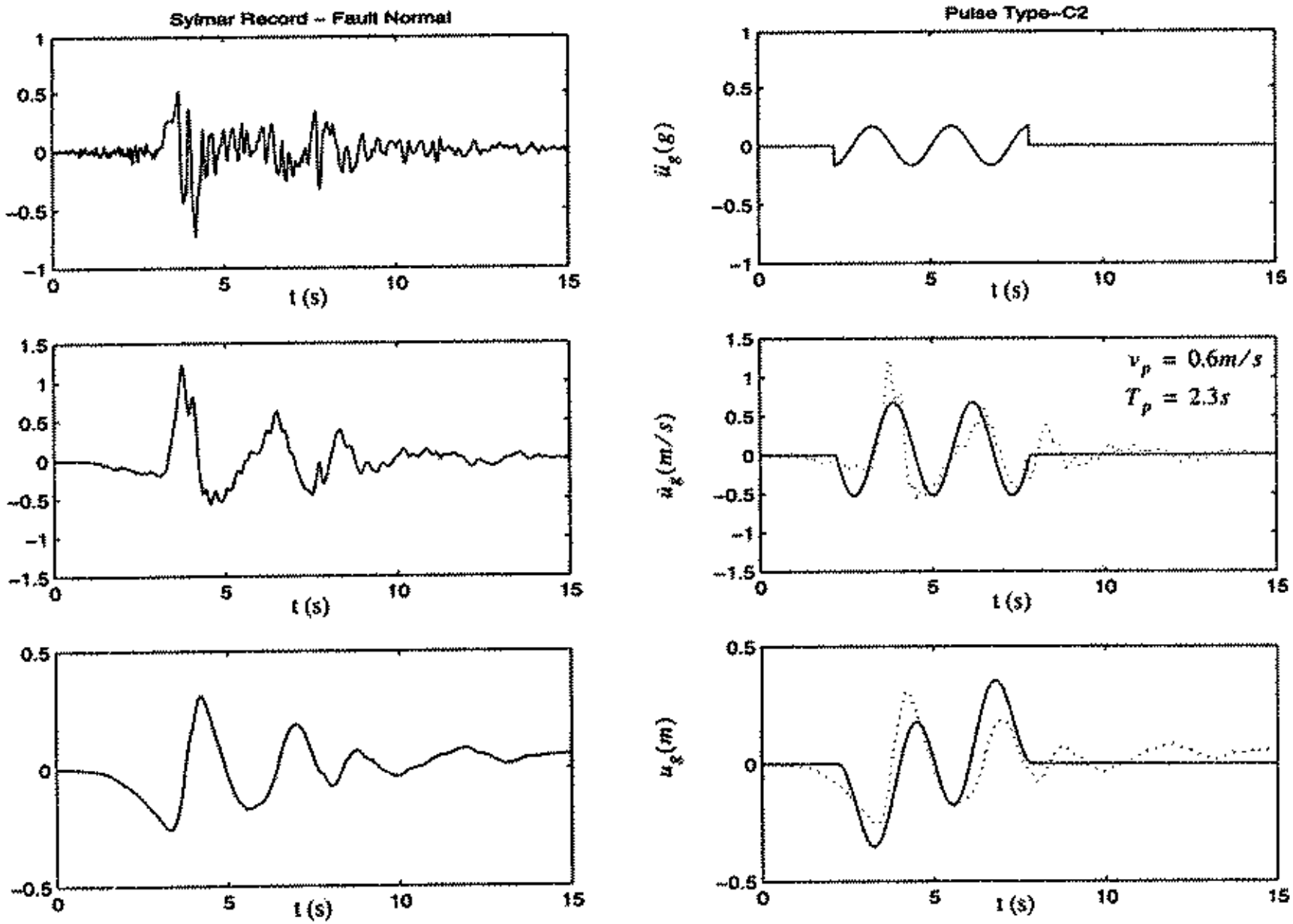

Figure 7: Fault normal components of the acceleration, velocity and displacement time histories recorded at the Sylmar station during the January 17th, 1994 Northridge, California earthquake (left) and a cycloidal type-C_2 pulse (right).

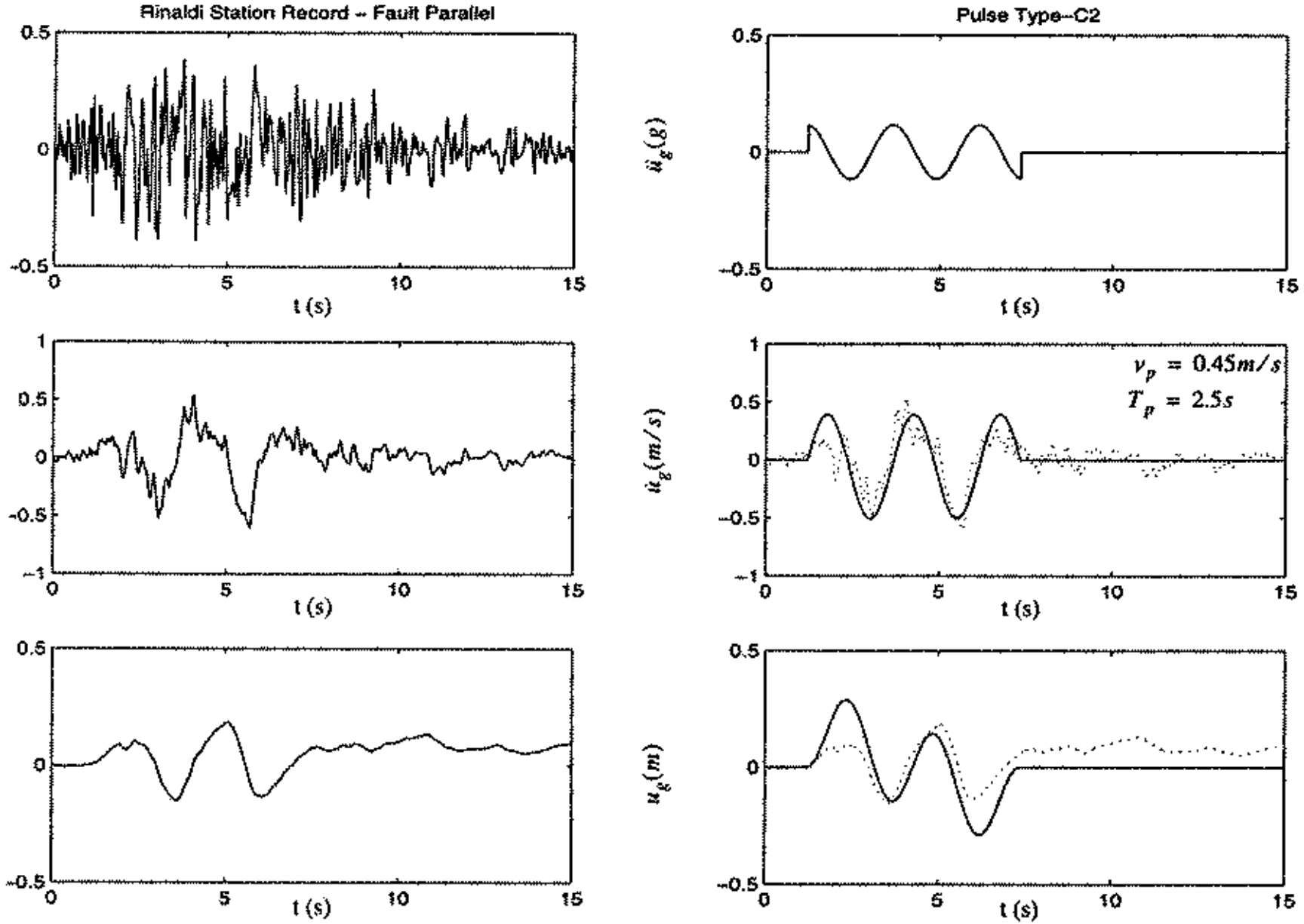

Figure 8: Fault parallel components of the acceleration, velocity and displacement time histories recorded at the Rinaldi station during the January 17th, 1994 Northridge, California earthquake (left) and a cycloidal type-C_2 pulse (right).

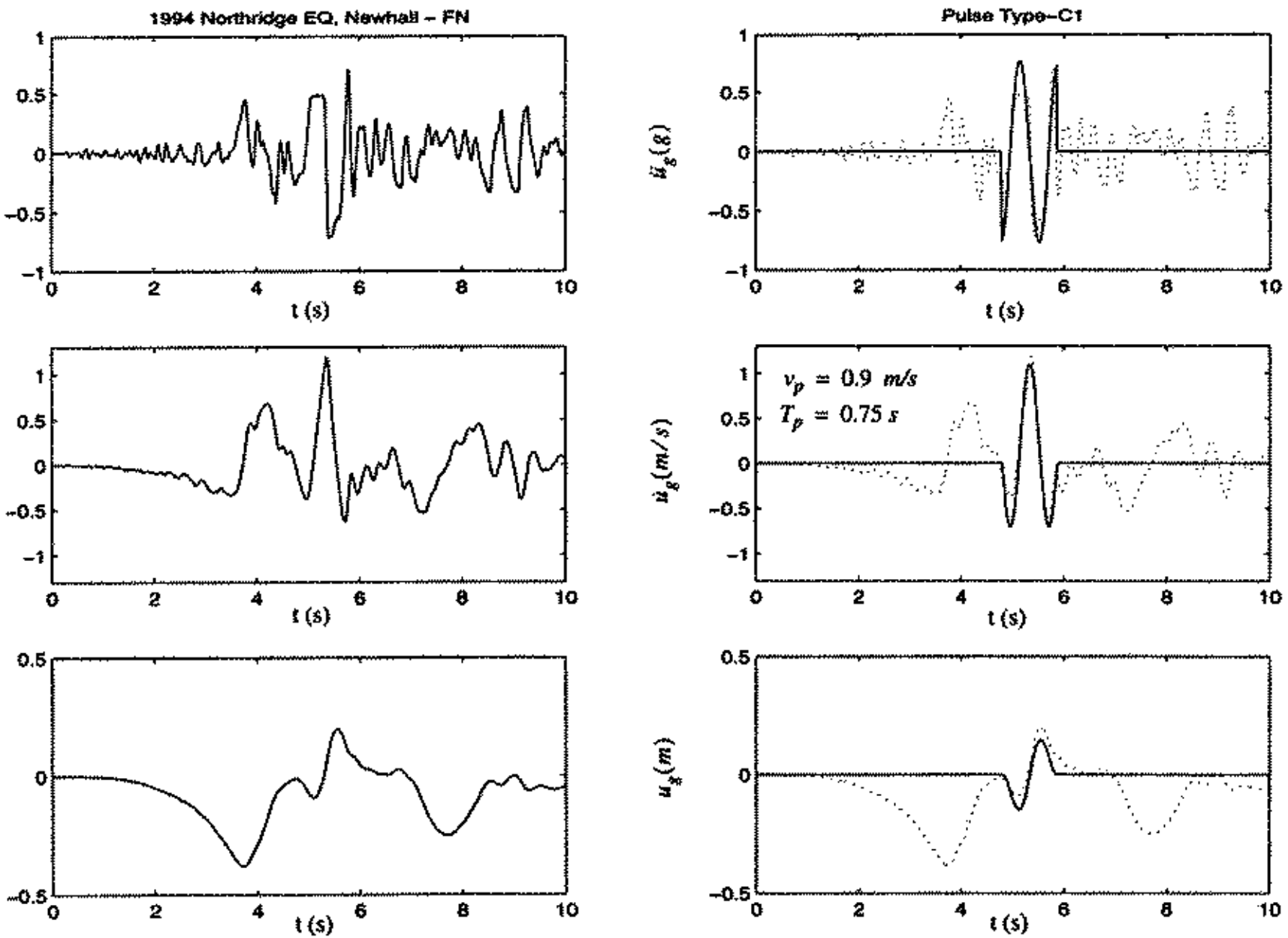

Figure 9: Fault normal components of the acceleration, velocity and displacement time histories recorded at the Newhall station during the January 17th, 1994 Northridge, California earthquake (left) and a cycloidal type-C_2 pulse (right).

$$\dot{u}_g(t) \;=\; v_p \sin(\omega_p t + \varphi) - v_p \sin(\varphi)\,,\; 0 \le t \le \left(n + \frac{1}{2} - \frac{\varphi}{\pi}\right) T_p\,, \tag{15}$$

$$u_g(t) \;=\; -\frac{v_p}{\omega_p}\cos(\omega_p t + \varphi) - v_p t \sin(\varphi) + \frac{v_p}{\omega_p}\cos(\varphi)\,,\; 0 \le t \le \left(n + \frac{1}{2} - \frac{\varphi}{\pi}\right) T_p\,. \tag{16}$$

In deriving these expressions it is required that the displacement and velocity are differentiable signals. The value of the phase angle, φ, is determined by requiring that the ground displacement at the end of the pulse be zero. A type-C_n pulse with frequency $\omega_p = 2\pi/T_p$ has duration $T = (n + 1/2)T_p - 2\varphi/\omega_p = (n + 1/2 - \varphi/\pi)T_p$. In order to have a zero ground displacement at the end of a type-C_n pulse

$$\int_0^{(n + 1/2 - \varphi/\pi)T_p} \dot{u}_g(t)\,dt \;=\; 0\,. \tag{17}$$

Equation (17), after evaluating the integral, gives

$$\cos[(2n + 1)\pi - \varphi] + [(2n + 1)\pi - 2\varphi]\sin\varphi - \cos\varphi \;=\; 0\,. \tag{18}$$

The solution of the transcendental equation given by (18) gives the value of the phase angle φ. For example, for a type-C_1 pulse (n = 1), $\varphi = 0.0697\pi$; whereas, for a type-C_2 pulse (n = 2), $\varphi = 0.0410\pi$. Figure 10 (third and fourth column) plots the acceleration, velocity and displacement histories of a type-C_1 and a type-C_2 pulse.

As n increases, a type-C_n pulse tends to a harmonic steady-state excitation. Figure 10 summarizes the acceleration, velocity and displacement shapes of a forward-pulse, a forward-and-back pulse, a type-C_1 and a type-C_2 pulse. The displacement of a forward-and-back pulse has the same shape as the velocity of a forward pulse. Similarly, the displacement of a type-C_1 pulse resembles the shape of the velocity of a forward-and-back pulse and the shape of the acceleration of a forward pulse. This shows that type-C pulses provide a continuous transition from cycloidal pulses to harmonic steady-state motions.

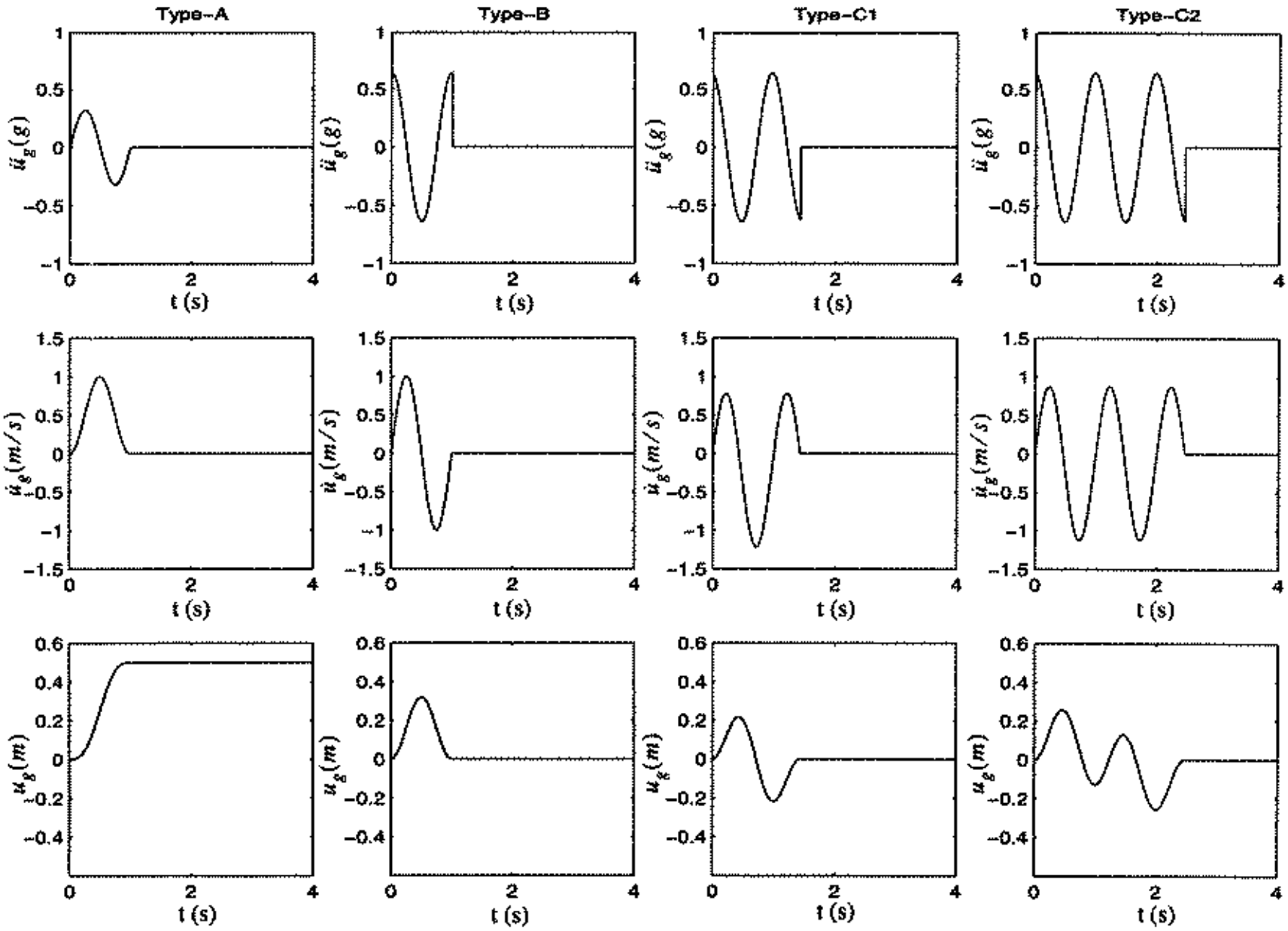

Figure 10: Acceleration, velocity and displacement time histories of cycloidal pulses type-A (first column), type-B (second column), type-C_1 (third column) and type-C_2 (fourth column).

CHAPTER 4

MODELING OF THE DISSIPATION MECHANISMS OF PRACTICAL ISOLATION SYSTEMS

In this study, we consider an isolated structure with a linear restoring force with stiffness, K_I, and various dissipation mechanisms which are approximated with idealized macroscopic models. Figure 11 shows the force-displacement loops of five dissipation mechanisms: (a) viscous model (high damping rubber bearings without or with viscous fluid dampers); (b) rigid-plastic model (sliding bearings); (c) elastic-plastic model (lead rubber bearings); (d) viscoplastic model (sliding bearings and viscous fluid dampers, elastomeric bearings and friction dampers, elastomeric bearings and controllable fluid dampers, sliding bearings and controllable fluid dampers); (e) elastoviscoplastic model (lead rubber bearings without or with viscous dampers).

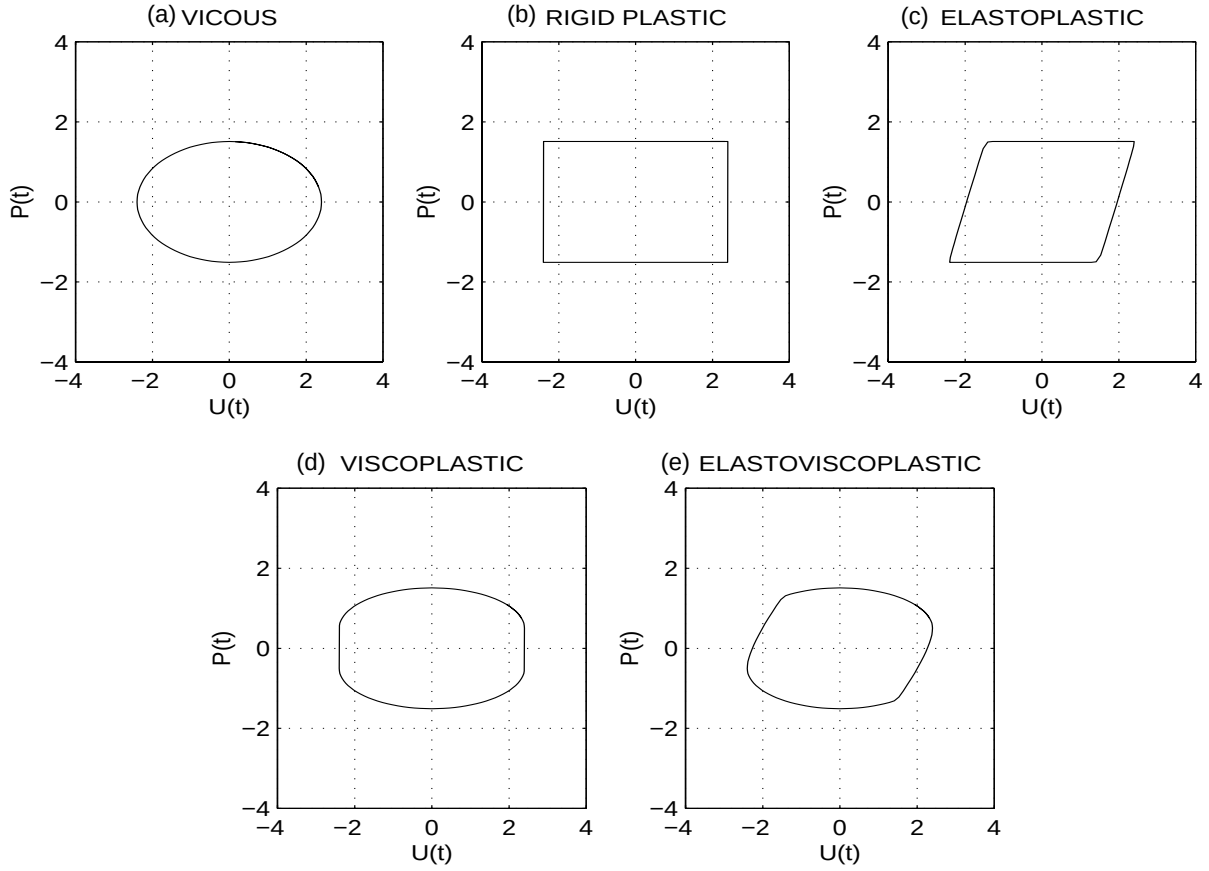

Figure 11: Five idealizations of energy dissipation mechanisms of practical seismic isolation systems.

It is worth mentioning that case 2 is the limiting case of 3, where the yield displacement becomes very small, whereas case 2 is also the limiting case of 4, where the viscous component vanishes. Accordingly, the dissipative behavior of a sliding bearing is the limiting case of dissipative behavior of a lead rubber bearing with a very small yield displacement. The elastoviscoplastic case 5 is the most general case, and the dissipation force can be expressed mathematically with

$$P(t) = C_I \dot{u}_b(t) + K_l u_y z(t) , \tag{19}$$

where u_b is the base displacement shown in Figure 1 (bottom), K_l is some reference stiffness, u_y is the value of the yield displacement of the isolation system and z is a hysteretic dimensionless quantity that is governed by the following equation:

$$u_y \dot{z} + \gamma \left| \dot{u}_b(t) \right| z |z|^{n-1} + \beta \dot{u}_b(t) |z|^n - A \dot{u}_b(t) = 0 . \tag{20}$$

The model given by (19) and (20) is a special case of the Bouc-Wen model (Wen 1975, 1976) enhanced with a viscous term. In equation (20), β, γ, n and A are dimensionless quantities that control the shape of the hysteretic loop. It can be shown that when A = 1, parameter K_l in (19) becomes the pre-yielding elastic stiffness. As an example, in a lead rubber bearing, K_l is the stiffness of the lead core before yielding. Based on this observation, parameter A is set equal to one. C_I is the viscous damping coefficient of the isolation system $C_I = C_b + C_d$, where $C_b = 2\xi_b(m + m_b)\omega_I$ is the viscous damping originating from the elastomeric bearings, and $C_d = 2\xi_d(m + m_b)\omega_I$ is the viscous damping originating from possible additional damping devices.

For the special case of rigid viscoplastic behavior, the yield displacement $u_y \to 0$ and the pre-yielding stiffness $K_e \to \infty$ so that the product $u_y K_e \to P_y$, which is the finite yield force. Under these conditions, equation (19) reduces to the Bingham model of viscoplasticity (Shames and Cozzarelli 1992),

$$P(t) = C_I \dot{u}_b(t) + P_y \operatorname{sgn}[\dot{u}_b(t)], \tag{21}$$

in which $P_y = P_{by} + P_{dy}$, where $P_{by} = \mu(m + m_b)g$ is the yield (friction type) force originating from the sliding bearing, and P_{dy} is the yield force that might originate from additional damping devices such as controllable fluid dampers. When sliding teflon bearings are used, the pre-yield stiffness is large but finite. Accordingly, even for sliding teflon bearings, the behavior is elasto-

plastic with a small yield displacement ($u_y \approx 0.2$ mm, Mokha et al. 1988). For, lead-rubber bearing, the elastoplastic model is also appropriate; however, the yield displacement is of the order of centimeters. With reference to Figure 1b, the equation of motion of the 2-DOF system is expresses as follows (Kelly 1997):

$$\begin{bmatrix} 1 & \gamma_m \\ 1 & 1 \end{bmatrix} \begin{bmatrix} \ddot{u}_b(t) \\ \ddot{u}_s(t) \end{bmatrix} + \begin{bmatrix} 0 & 0 \\ 0 & 2\xi_s\omega_s \end{bmatrix} \begin{bmatrix} \dot{u}_b(t) \\ \dot{u}_s(t) \end{bmatrix} + \begin{bmatrix} \omega_b^2 & 0 \\ 0 & \omega_s^2 \end{bmatrix} \begin{bmatrix} u_b(t) \\ u_s(t) \end{bmatrix} + \begin{bmatrix} 1 \\ 0 \end{bmatrix} \alpha(t) = -\begin{bmatrix} 1 \\ 1 \end{bmatrix} \ddot{u}_g(t) \quad (22)$$

where $\gamma_m = m_s/(m + m_b)$ and $\alpha(t) = P(t)/(m + m_b)$, in which $P(t)$ is the dissipation force given by equation (19) or (21). The parametric analysis presented in this report is conducted by solving equation (22) for various representations of the dissipative force $P(t)$.

The response of the 2-DOF structure shown in Figure 1 (bottom), which is expressed with (22), is computed using a state-space formulation where the state vector of the system is $y(t) = \langle u_b(t), \dot{u_b}(t), u_s(t), \dot{u_s}(t), z(t) \rangle^T$. The seismic response of isolated overpasses like the one shown in Figure 12 is computed by setting the natural frequency of the superstructure to be very large.

CHAPTER 5

PARAMETRIC STUDY

The formulation presented in the previous section is first used to predict the response of a 1-DOF overcrossing shown in Figure 12. Figure 12 (top) depicts an overcrossing that is isolated at the center bent and end-abutments. Figure 12 (bottom) depicts an overcrossing that is rigidly connected to its center bent and supported on isolation bearings at the end-abutments. Typical values of isolation periods range from T_I = 2 sec or more for the top configuration, down to T_I = 1 sec or even less for the bottom configuration.

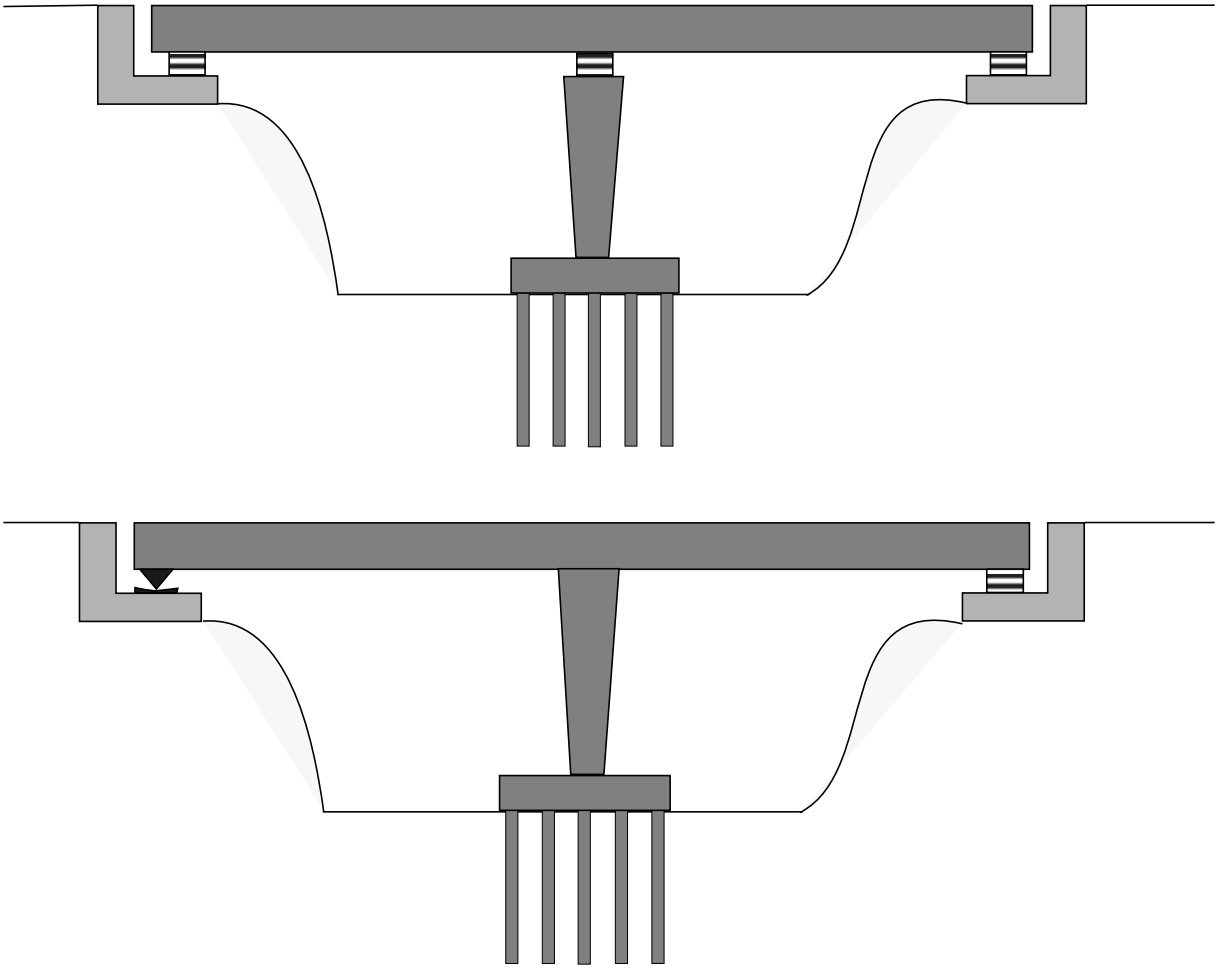

Figure 12: Schematic of a seismically isolated overpass (top) and of an overpass that is supported on bearings at the end abutments (bottom)**.**

The scope of this parametric study is to provide information on the efficiency of various combinations of dissipation mechanism to suppress the earthquake response. First, various levels of viscous damping alone are considered. Subsequently, various levels of friction (plastic) forces are considered where: (a) the yield displacement is very small ($u_y \approx 0.2$ mm) and; (b) the yield displacement is finite ($u_y = 10$ mm and 20 mm). This distinction is of interest in order to observe potential differences between a "rigid" plastic and an elastic plastic model that will reflect the behavior of a teflon sliding bearing and a lead rubber bearing respectively with the same yield force. When viscous damping alone is considered, the levels of viscous damping in the isolation system have been chosen to be ξ_I = 5%, 15% and 30%. Isolation systems with ξ_I = 15% are common; whereas, ξ_I = 30% is at the high end. The levels of the coefficient of friction selected in this study are μ = 6%, 9% and 18%. Values of μ = 6% and 9% are typical values of friction coefficients on commercially available sliding bearings. Similar levels of yield forces can be reached with lead rubber bearings. The value of μ = 18% was selected to illustrate the effects of high-value dry friction. A parametric study is also conducted to identify the improvement in the response when additional viscous damping is combined with hysteretic damping that originates from a plastic force with μ = 9%.

The first column on Figure 13 shows the response of a 1-DOF overcrossing with isolation period T_I = 2 sec and viscous isolation damping ξ_I = 15% subjected to the type-A cycloidal front with T_p = 1.0 sec and the Rinaldi station record shown in Figure 5. For the type-A pulse (first and second row), relative displacements reach 50 cm (20 in); whereas the base shear coefficient exceeds the value of 0.5. The second column in Figure 13 plots the response of the isolated structure where the isolation damping has been doubled by adding viscous dampers, $\xi_I = \xi_b + \xi_d$ = 30%. With a total isolation damping coefficient of ξ_I = 30%, the base displacement reduces by 30% (35 cm) and the base shear reduces by 15%. The reason that the base shear reduces under the presence of twice the viscous damping is because, although additional damping increases the damping forces, it decreases displacements, resulting in smaller elastic forces.

We are now interested in computing the effective damping coefficient of the 1-DOF system during this shaking. Under a pulse excitation with duration smaller than the natural period of a structure, its vibration period is very close to its natural period. Indeed, the top graphs of all columns of Figure 13 clearly show that the 1-DOF system completes a cycle within 2 sec = T_I.

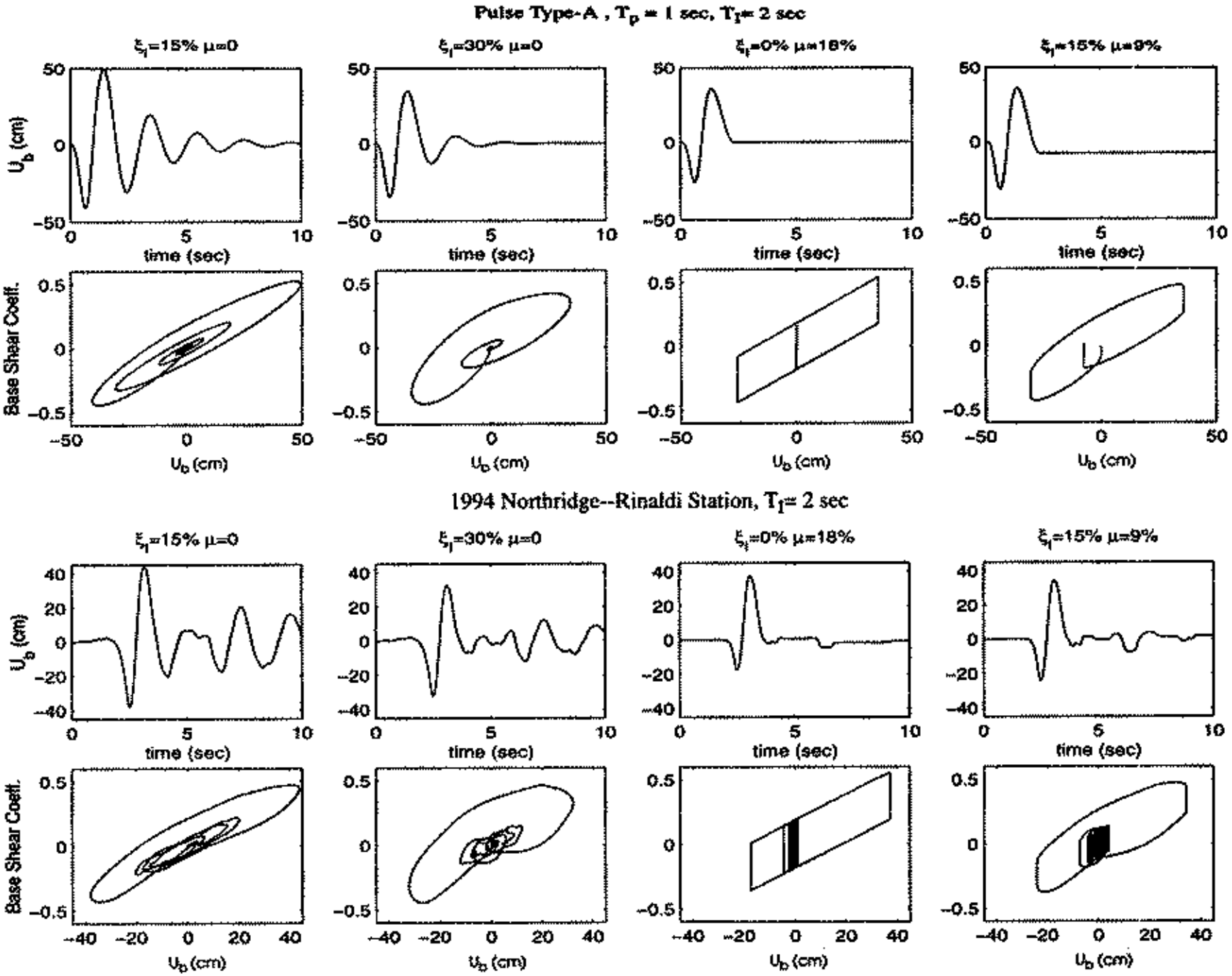

Figire 13: Response quantities of an isolated block with T_i = 2 sec subjected to a type A pulse with T_I = 1sec (top) and to the Rinaldi station record (bottom)

Consequently, $\Omega = \omega_I$, and according to equation (4), the effective damping coefficient should be $\beta_{eff} = \xi_I = 15\%$ for the response shown in the first column, and $\beta_{eff} = \xi_I = 30\%$ for the response shown in the second column. The area of the loops shown in the second row is equal to $\overline{W}_D = W_D/(mg)$, and equation (3) allows for a direct measurement of the resulting effective damping coefficient, which is given by

$$\beta_{eff} \approx \frac{1}{2\pi} \frac{\overline{W}_D g}{\omega_I^2 D^2} , \tag{23}$$

where $D = (|u_{min}| + |u_{max}|)/2$. Equation (23) gives a value of $\beta_{eff} \approx 0.20$ for the response shown in the first column, and a value of $\beta_{eff} \approx 0.37$ for the response shown in the second column. These values are 30% and 20% larger than the corresponding values obtained with equation (4). The reason for this discrepancy is that the definitions of ξ and β_{eff} given by equation (2) and (3) are for harmonic-steady-state vibrations and not for transient motions, like those shown at the top of Figure 13.

The third column in Figure 13 plots the response of the isolated structure where the isolation damping is only of the friction type (rigid-plastic damping). It is shown that, for this system, ($T_I = 2$ sec); a coefficient of friction $\mu = 18\%$ is needed to achieve the same displacement reduction that a 30% viscous coefficient achieves. When the dissipation is due to friction only (rigid-plastic), $P(t) = \mu mg\,\mathrm{sgn}[\dot{u}_b(t)]$, and equation (3) simplifies to

$$\beta_{eff} \approx \frac{2\mu g}{\pi \omega_I^2 D} = \frac{2\alpha_y}{\pi \omega_I^2 D} . \tag{24}$$

For the loop shown in the third column of Figure 13, equation (24) gives $\beta_{eff} = 38\%$, which is approximately the same amount of effective damping coefficient that resulted from the viscously damped structure. The last column in Figure 13 plots the response of the isolated structure that combines viscous damping, $\xi_I = 15\%$, and friction damping that corresponds to $\mu = 9\%$. This combination of viscous and friction damping achieves the same displacement reduction that was achieved with the two other configurations. Furthermore, equation (23) results in an effective damping coefficient, $\beta_{eff} = 38\%$, which is comparable to the values of β_{eff} that resulted from the two other systems.

Figure 13 (bottom) shows the response of the same 1-DOF system with T_I = 2 sec when excited by the Rinaldi station record. With viscous isolation damping ξ_I = 15%, the maximum displacement is 44 cm which is 17% less than the maximum displacement reached under a type-A pulse front with nearly the same velocity pulse. The increase of the isolation damping from ξ_I = 15% to ξ_I = 30% reduced the response from 44 cm to 32.4 cm --- a 30% reduction, which is the same amount of reduction that is achieved in the case of a pulse type-A motion.

The third column in Figure 13 plots the response of the 1-DOF system under rigid-plastic dissipation (μ = 18%). It is interesting to note that the maximum displacement is 37.4 cm, which is more than the displacement that was reached under a type-A pulse motion (see first row in Figure 13), although now the resulting β_{eff} = 42%. Furthermore, the value of μ = 18% now results in a 5 cm larger displacement response than the response obtained with ξ_I = 30%, and a 20% larger base shear. Consequently, this example shows that two systems which are equivalent under one input exhibit opposite trends under a different but similar input, and that the concept of effective damping coefficient has little meaning since its value is strongly response-dependent.

Figure 14 shows the response of a 1-DOF system with isolation period T_I = 1 sec when subjected to the type-A cycloidal front with T_p = 1.0 sec and the Rinaldi station record. Now the relative displacement reaches 30 cm (12 in), whereas the base shear coefficient exceeds the value of 1.2. The second column plots the response of the isolated structure, where now the viscous damping of the isolation system is ξ_I = 30%. Again the same trends are observed, where the addition of viscous damping reduces both displacements and base shear. The third column in Figure 14 plots the response of the isolated structure with friction type (rigid-plastic damping) only, using the same value of friction coefficient (μ = 18%). All displacements and base shear coefficients in the third column are larger than the corresponding values in column 2. Column 4 plots the response of the isolated structure that combines viscous damping, ξ_I = 15%, and friction damping that corresponds to μ = 9%.

The seismic performance of the rigid block equipped with various types of damping mechanisms in its isolation system is summarized in Figure 15, where displacement and base shear spectra are plotted for the fault normal component of the Rinaldi station record (left), a type-A pulse excitation with T_p^A = 0.8 sec (center) and a type-B pulse excitation with T_p^B = 1.3 sec (right), and kinematic characteristics that approximate those of the Rinaldi station record. It is observed

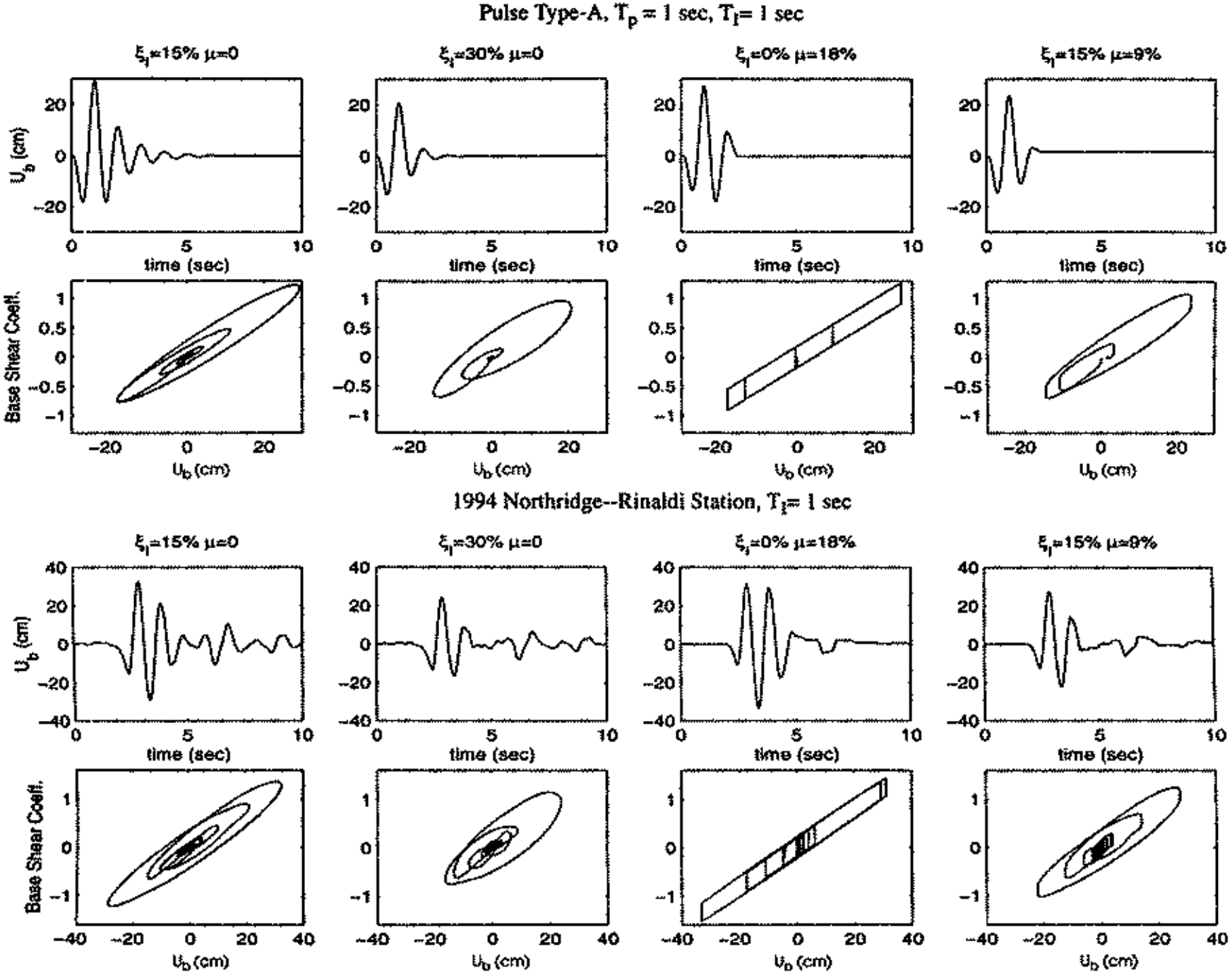

Figure 14: Response quantities of an isolated block with T_I = 1 sec subjected to a type A pulse with T_I = 1sec (top) and to the Rinaldi station record (bottom)

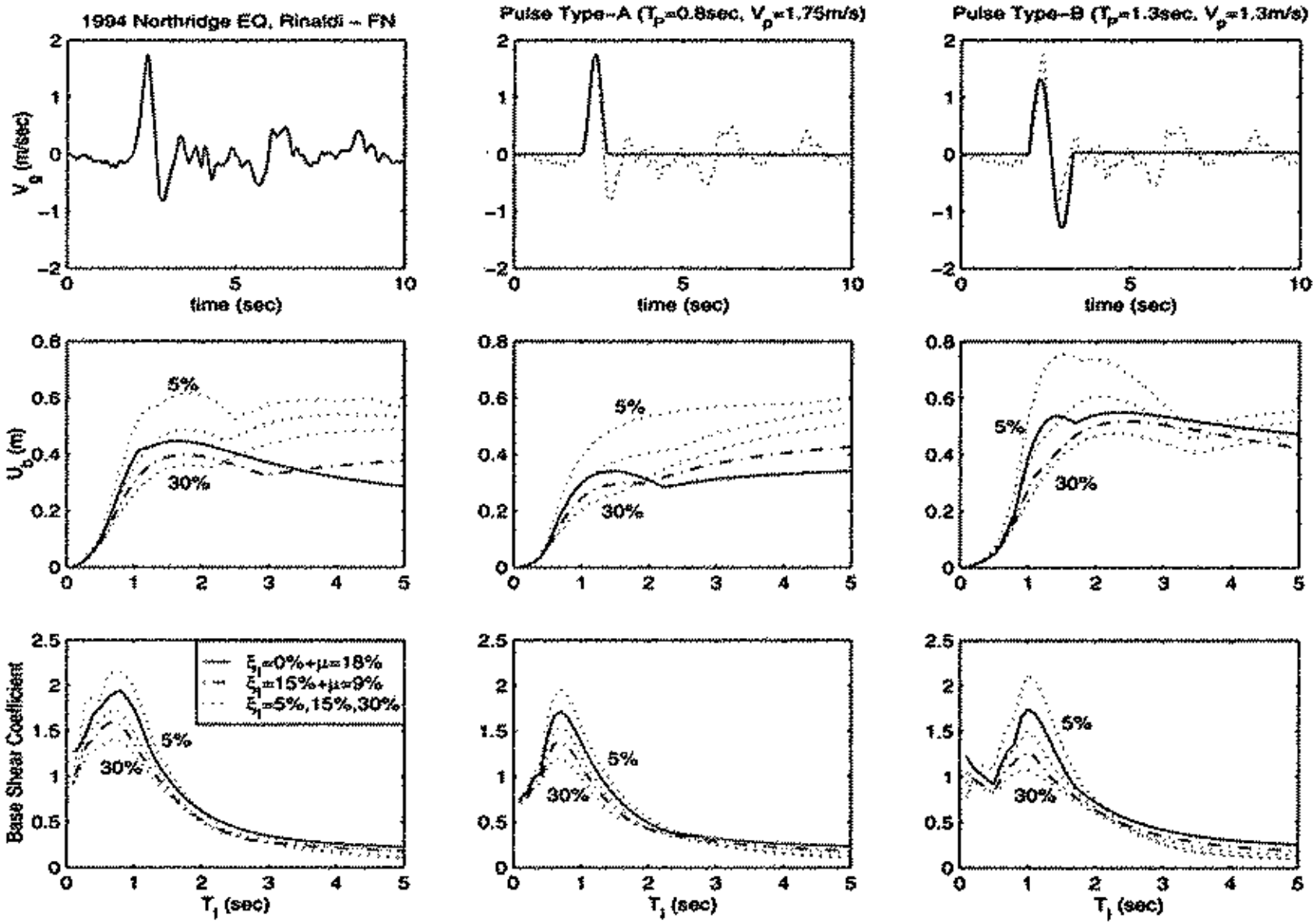

Figure 15: Displacement and base shear spectra of an isolated block subjected to the fault normal component of the Rinaldi station record (left), a type-A pulse (center) and a type-B pulse (right).

that, at the low isolation period range (i.e., T_I < 2.0 sec), additional viscous damping reduces the displacements and base shear in the most effective way. Friction dissipation alone (ξ_I = 0, μ = 18%) becomes effective in reducing displacement at large isolation periods, however, the resulting base shear is the largest. A combination of viscous and friction damping results in an attractive performance, since the effective reduction of displacements is accompanied by base shear lower than that resulting from friction dissipation alone. For example, Figure 15 (left) indicates that an isolation period T_I = 3.0 sec with ξ_I = 15% and μ = 9% will result to a base displacement of u_b = 33 cm and a base shear coefficient of 0.25. On the other hand, additional energy dissipation devices that will increase the damping of a 1 sec period structure from 5% to 30% will reduce displacement to half; whereas the base shear will exceed the weight of the structure. Another interesting observation is that the response spectra of the fault normal component of the Rinaldi station record has a smooth shape, resembling the shape of the spectra obtained with the pulse type-A and pulse type-B excitations.

Figure 16 plots the displacement and base shear spectra of the fault normal component of the Rinaldi station and for three different values of yield displacements (left: u_y = 0.2 mm, center: u_y = 10 mm, right: u_y = 20 mm). Two values of the yield force, $F_y = \mu W$, (W is the above-the-isolation system mass) have been selected (μ = 6% and μ = 9%). Figure 16 shows that the value of the yield displacement has insignificant effect on the values of base displacements and base shears. Accordingly, rigid-plastic behavior (sliding bearings) results to nearly the same response reduction as elastic-plastic behavior (lead rubber bearings) provided that both systems have the same yield force, $F_y = \mu W$. In the absence of viscous dissipation (ξ_I = 0), an increment of the plastic (yield) force from 6% to 9% suppresses further resonant effects. However, under the presence of viscous force (ξ_I = 15%), the increase of the plastic force from 6% to 9% has a minor effect in both base displacements and base shears.

The parametric study presented herein also investigates the influence that supplemental viscous damping has on the response reduction assuming a nominal value of plastic forces. Several recently constructed isolated buildings and bridges combine isolation bearings and fluid dampers. For instance, the San Bernadino Medical Hospital combines high damping rubber bearings and hydraulic fluid dampers; while, the Hayward City Hall combines friction pendulum sliders and hydraulic fluid dampers.

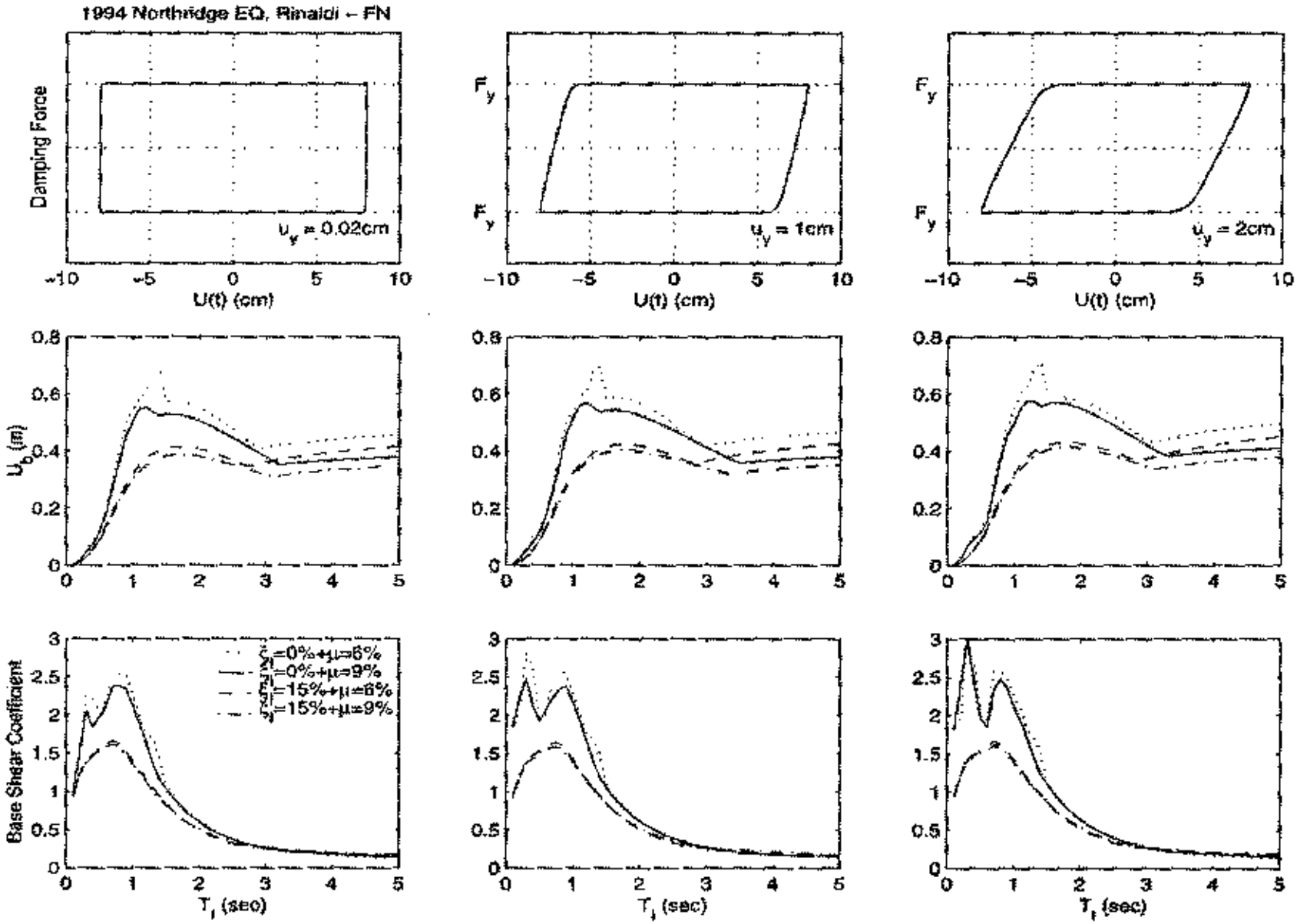

Figure 16: Displacement and base shear spectra of an isolated block subjected to the fault normal component of the Rinaidi station record. Left: u_y = 0.2 mm; center: u_y = 10 mm; right: u_y = 20 mm.

Figure 17 shows that under the Rinaldi station record an isolation system with T_I = 2 sec and plastic dissipation only (ξ_I = 0 and μ = 9%), will experience displacement that exceeds 50 cm. An additional 15% of viscous damping reduced the displacement to 40 cm which is an additional 20% reduction. Figure 17 shows that for a longer isolation period, say T_I = 3 sec, the additional benefit from the supplemental viscous damping is marginal.

Figure 18 plots the displacement and base shear spectra of the fault normal component of the Lucerne Valley record (left), a type-A pulse with T_p^A = 3 sec (center) and a type-B pulse with T_p^B = 5 sec (right). In this case, friction dissipation alone results in the smallest displacement values; whereas, the combination of viscous and friction damping results in the smallest base shear values. In the low range of isolation periods (T_I < 2.0 sec), the spectrum from the recorded motion is substantially different from the spectrum that results from the pulse motions, indicating that, in the low isolation period range the response is governed by the high frequency fluctuations that override the long duration pulse. At the high range of isolation period (T_I > 2.0 sec), viscous dissipation results in large displacements that are substantially reduced when some friction dissipation is introduced. Again, a 3 sec isolation period with ξ_I = 15% and μ = 9% results in an attractive design. Figure 19 shows the same response quantities for three different values of yield displacements (u_y = 0.2 mm, 10 mm and 20 mm). Again, rigid-plastic behavior (sliding bearings) results to nearly the same response reduction as elastic-plastic behavior (lead rubber bearings). It is observed that in this case, the increase of plastic forces from μ = 6% to μ = 9% has a noticeable effect under the absence and presence of viscous forces. Figure 19 also indicates that pure friction damping with μ = 9% has the same effect as viscoplastic damping with μ = 6% and ξ_I = 15%. Furthermore, the increase of viscous damping from ξ_I = 0 to ξ_I = 15% has less drastic effects as the value of plastic dissipation increases.

Figures 20 and 21 illustrate the effects of the high-frequency fluctuations that override the long duration pulse. Under the Caleta de Campos and the Lucerne Valley forward motions, the base shear that develops in the long period structures when friction dissipation is included is larger than the base shear resulting from viscous dissipation. In contrast, when the long duration pulse is considered alone (right graphs), the trend is reversed.

Figure 22 plots the displacement and base shear spectra of the fault normal component of the El Centro Array #5 record (left) and a type-B pulse with T_p^B = 3.2 sec (right). In this case,

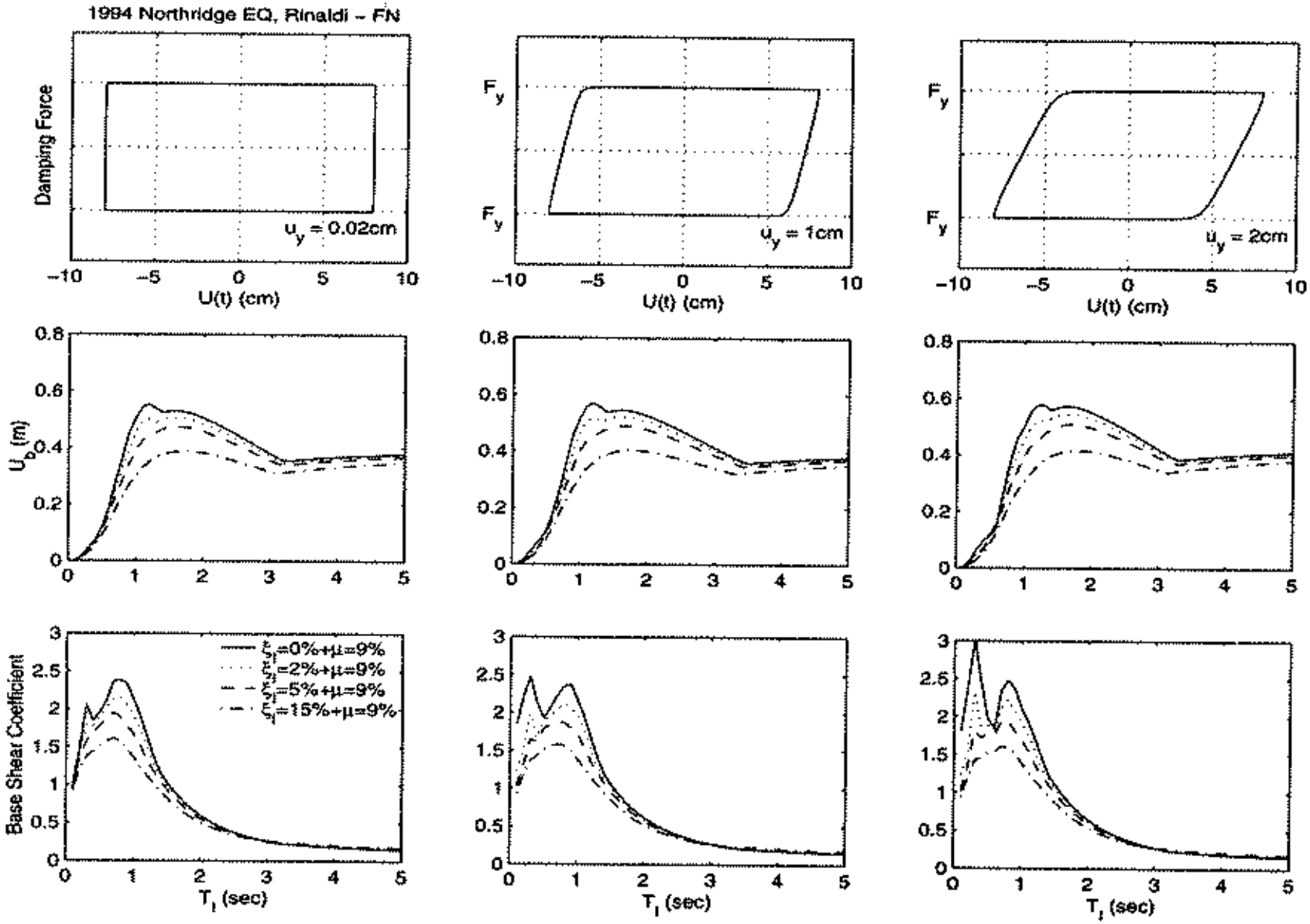

Figure 17: Displacement and base shear spectra of an isolated block subjected to the fault normal component of the Rinaldi station record. Left: $u_y = 0.2$ mm; center: $u_y = 10$ mm; right: $u_y = 20$ mm.

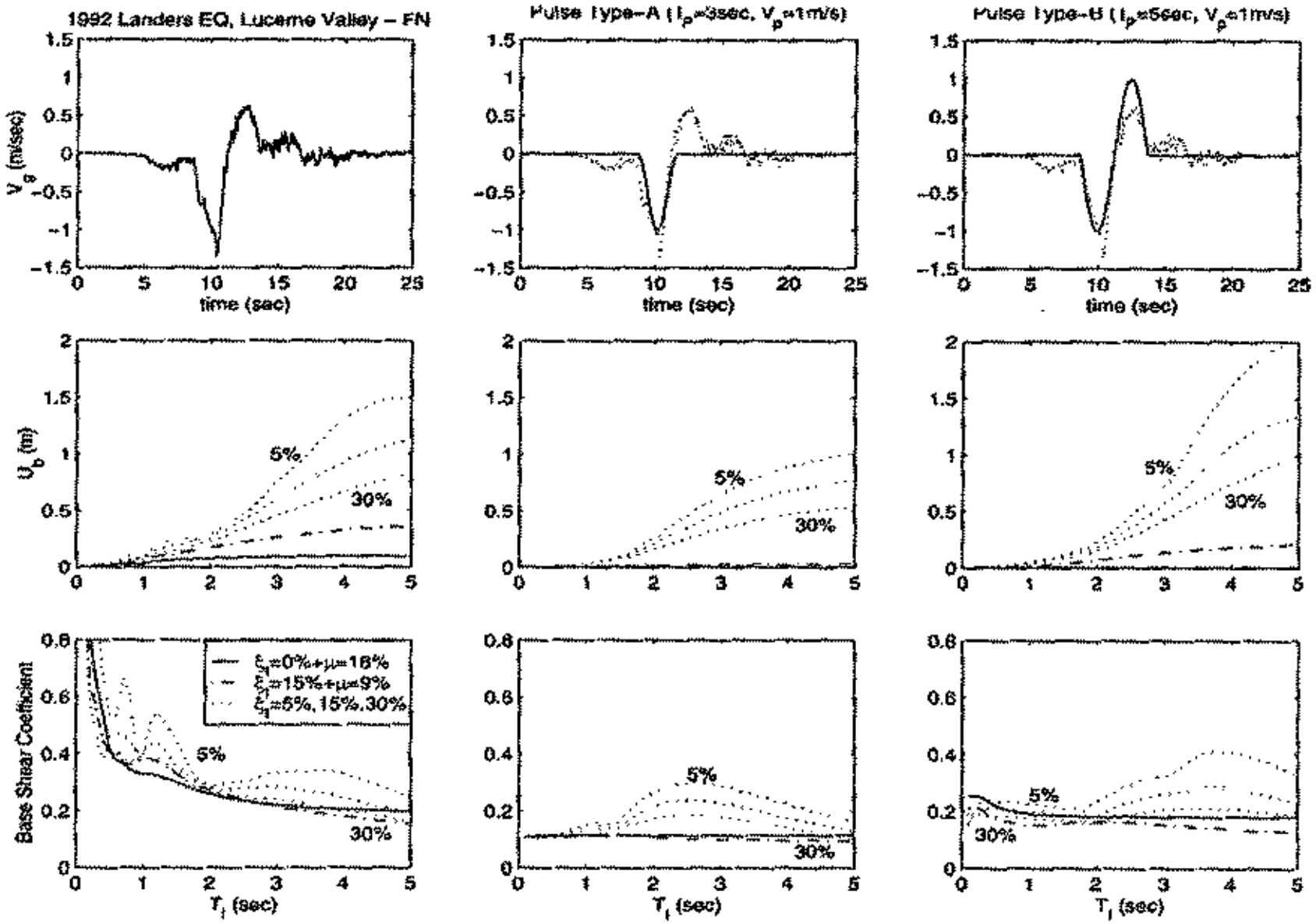

Figure 18: Displacement and base shear spectra of an isolated block subjected to the fault normal component of Lucerne Valley record (left), a type-A pulse (center) and a type-B pulse (right).

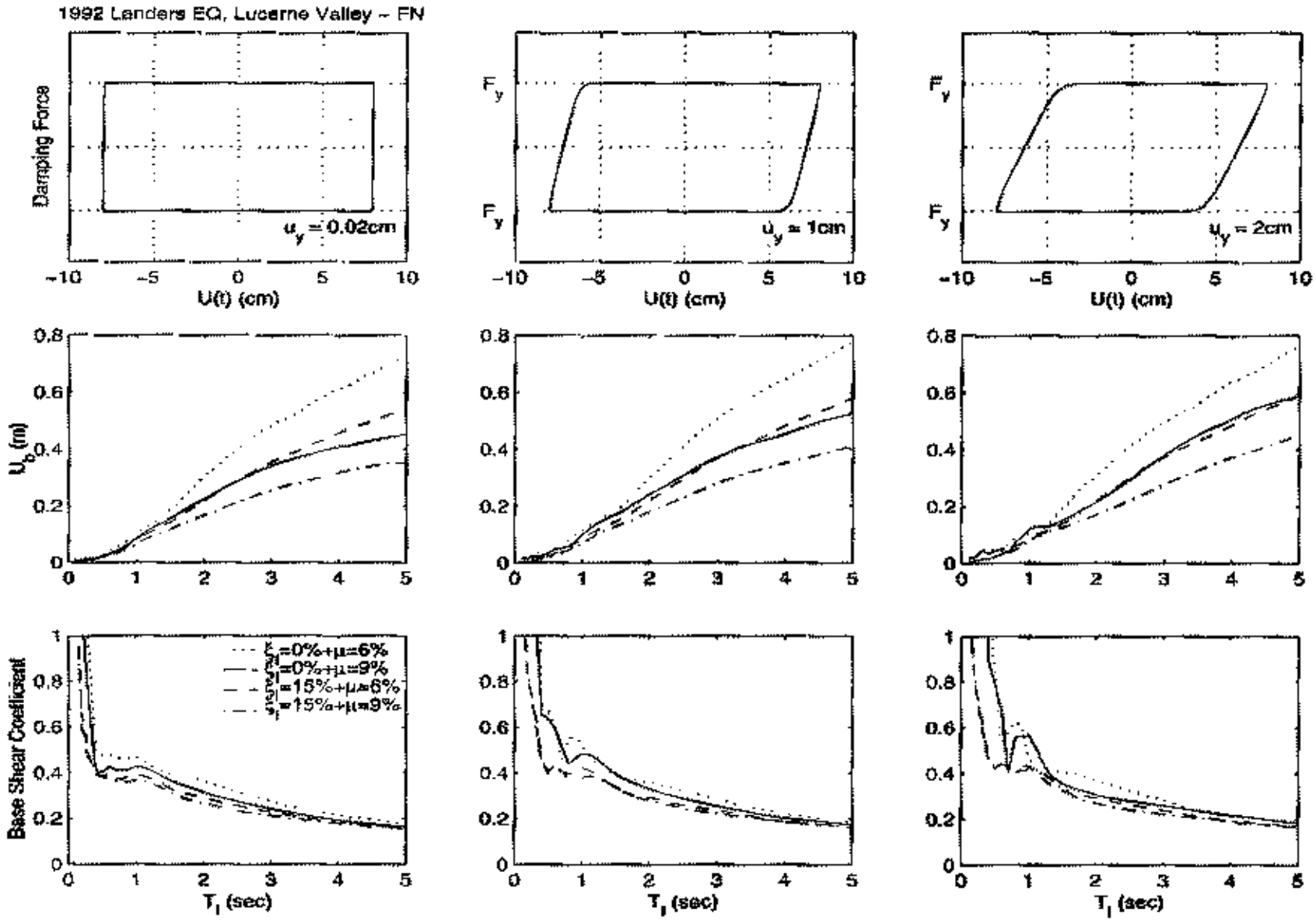

Figure 19: Displacement and base shear spectra of an isolated block subjected to the fault normal component of the Lucerne Valley record. Left: $u_y = 0.2$ mm; center: $u_y = 10$ mm; right: $u_y = 20$ mm.

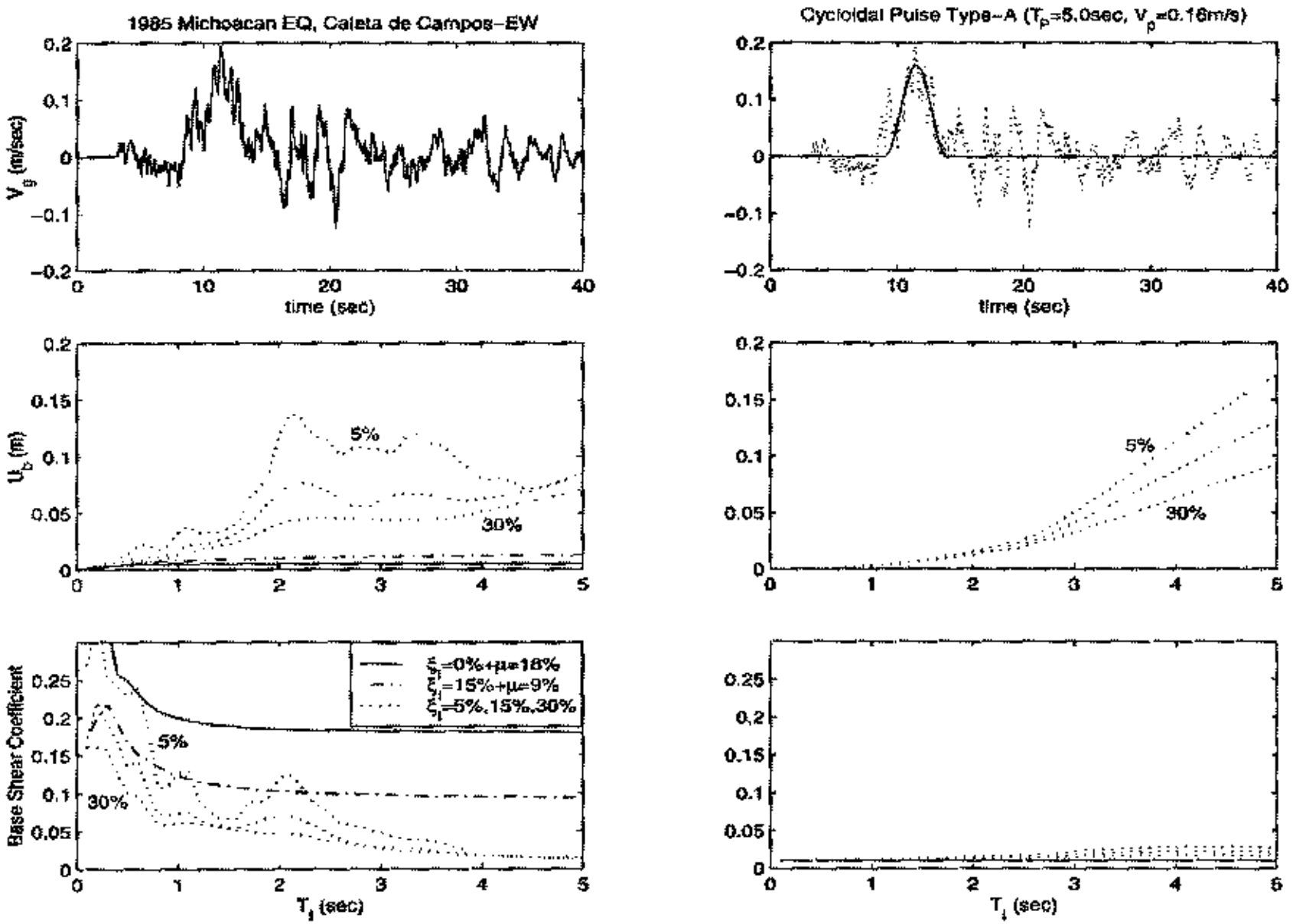

Figure 20: Displacement and base shear spectra of an isolated block subjected to Caleta de Campos record (left) and a type-A pulse (right).

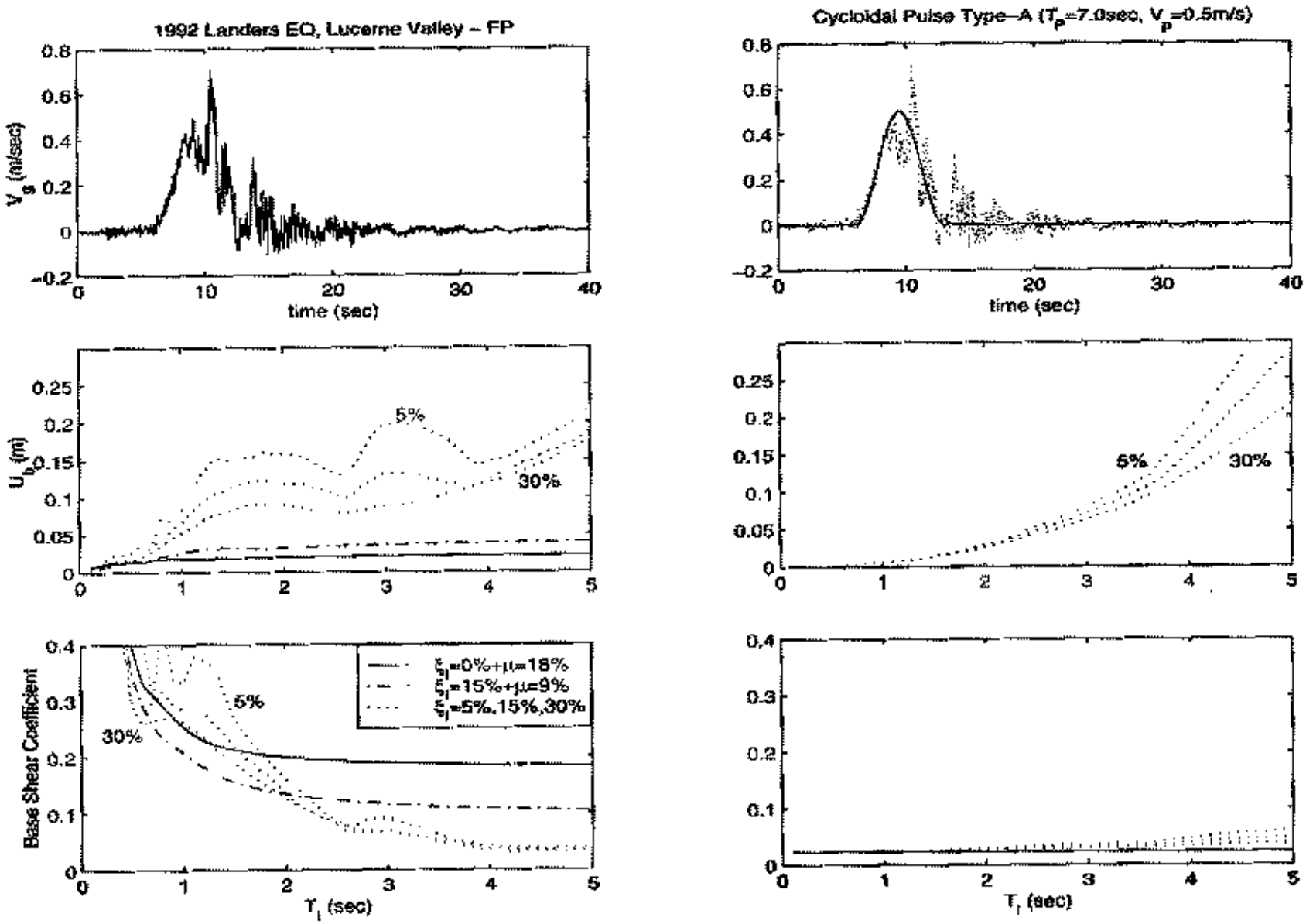

Figure 21: Displacement and base shear spectra of an isolated block subjected to the fault parallel component of Lucerne Valley record(left) and a type-A pulse (right).

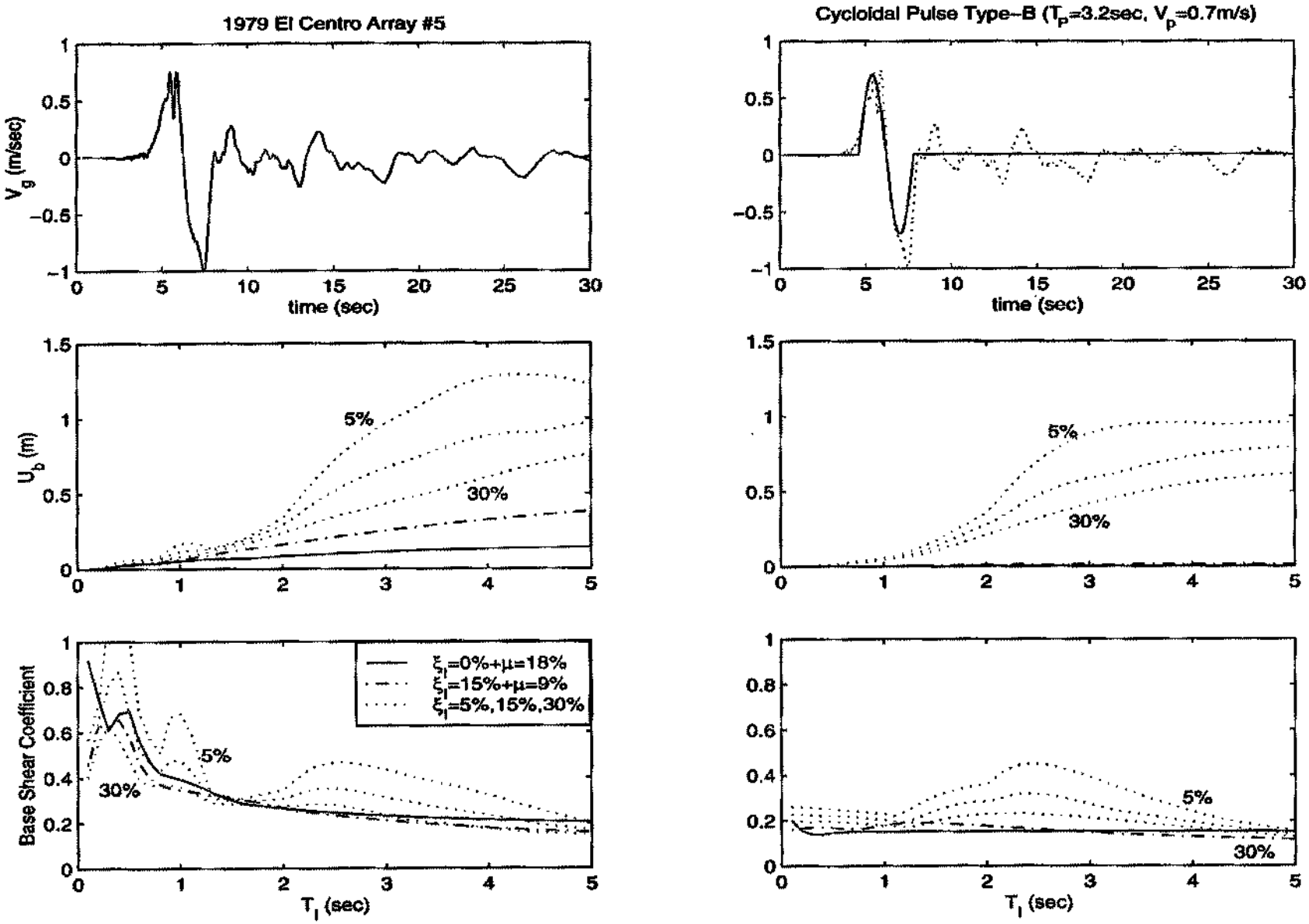

Figure 22: Displacement and base shear spectra of an isolated block subjected to the El Centro Array #5 station record (left) and a type-B pulse (right).

viscous dissipation results not only in large displacement, but also in substantial base shear. Friction dissipation eliminates amplification due to resonance for isolation periods longer than 2 sec. A 3 sec isolation period with ξ_I = 15% and μ = 9% again results in an attractive response, showing that there is no need for an extremely long isolation period (i.e., T_I =5 sec) to protect structures from near-source ground motions. Figure 23 shows similar trends to those observed in Figure 19. The improvement of the response when viscous damping is augmented from 0% to 15% is much more dramatic when plastic forces are of the order of 6%. When plastic forces are of the order of 9%, the improvement of adding substantial viscous damping is less noticeable.

Figure 24 plots the displacement and base shear spectra of the fault normal component of the Sylmar record (left) and a type-C_2 pulse with $T_p^{C_2}$=2.3 sec (right). The sensitivity of the response on the level of yield displacement is shown on Figure 25. Trends similar to those detected in Figure 16 are observed in this case. In the absence of viscous dissipation (ξ_I = 0), an increment of the plastic (yield) force from 6% to 9% suppresses further resonant effects; however, under the presence of viscous force (ξ_I = 15%), the increment of the plastic (yield) force from 6% to 9% has a less drastic effect. On the other hand, when a nominal value of plastic forces, of the order of 9% has been selected, supplemental viscous damping has a noticeable effect only at large values of the isolation period.

Figure 26 shows that under the Sylmar record adding supplemental damping has noticeable effects even for the level of plastic forces of the order of μ = 9%. This observation indicates that various designs can result into a meaningful isolation system. Either fluid damper should be added to reduce displacements or larger isolators should be designed to accommodate the larger displacements. In such situation, the selection of the most appropriate isolation system will be influenced from economic factors.

Figure 27 confirms the beneficial effect of hysteretic dissipation to suppress displacement and base shear when the predominant long period of the seismic input is near the isolation period of the structure. The moderate values of plastic and viscous forces (μ = 9% and ξ_I = 15%) are sufficient to totally suppress base displacements and base shears. The same trends are observed in Figures 28 and 29 which also indicate that there is no need for extremely long isolation periods to reduce appreciable base shears.

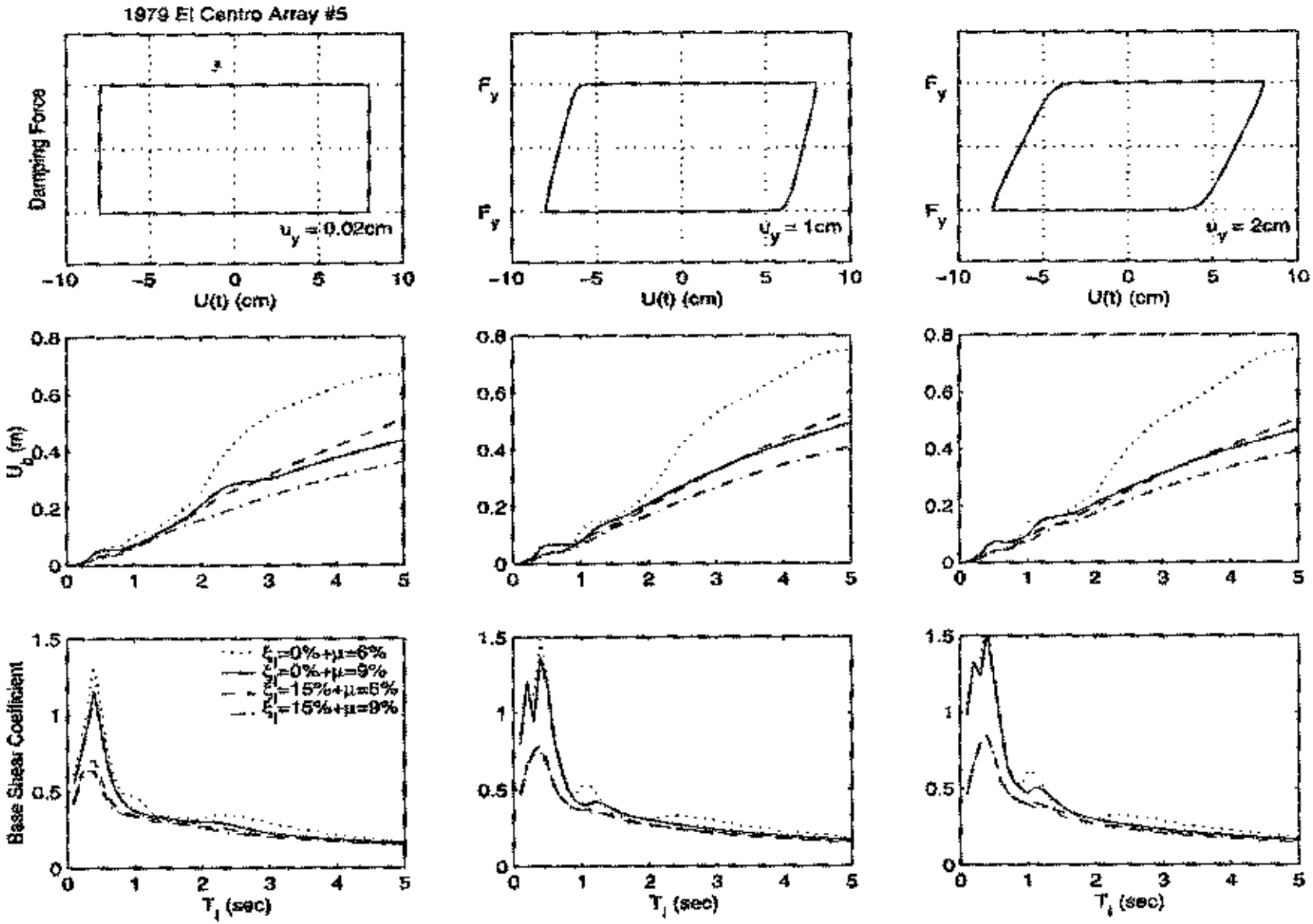

Figure 23: Displacement and base shear spectra of an isolated block subjected to the fault normal component of the El Centro Array #5 station record. Left: $u_y = 0.2$ mm; center: $u_y = 10$ mm; right: $u_y = 20$ mm.

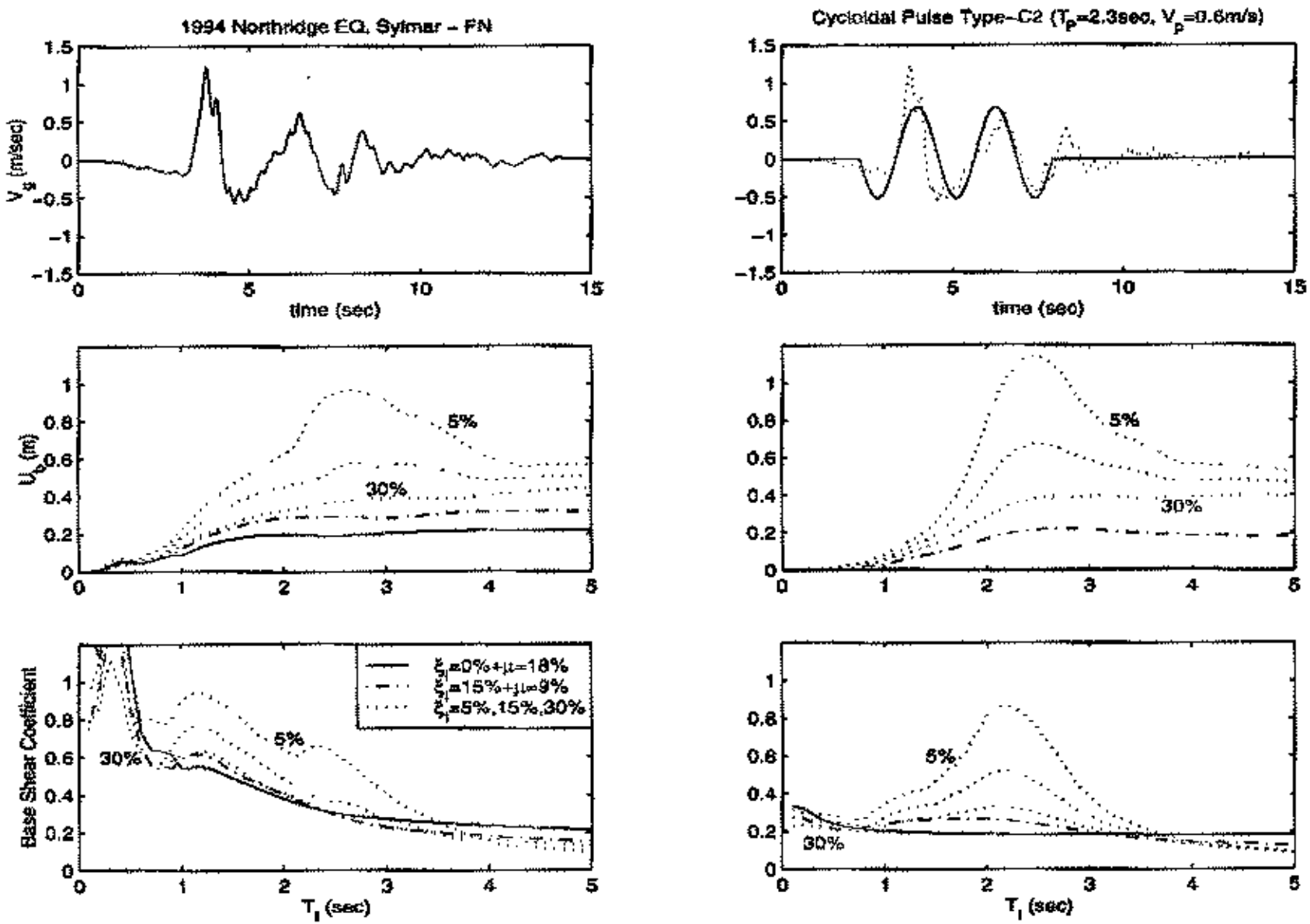

Figure 24: Displacement and base shear spectra of an isolated block subjected to the Sylmar station record (left) and a type-C_2 pulse (right).

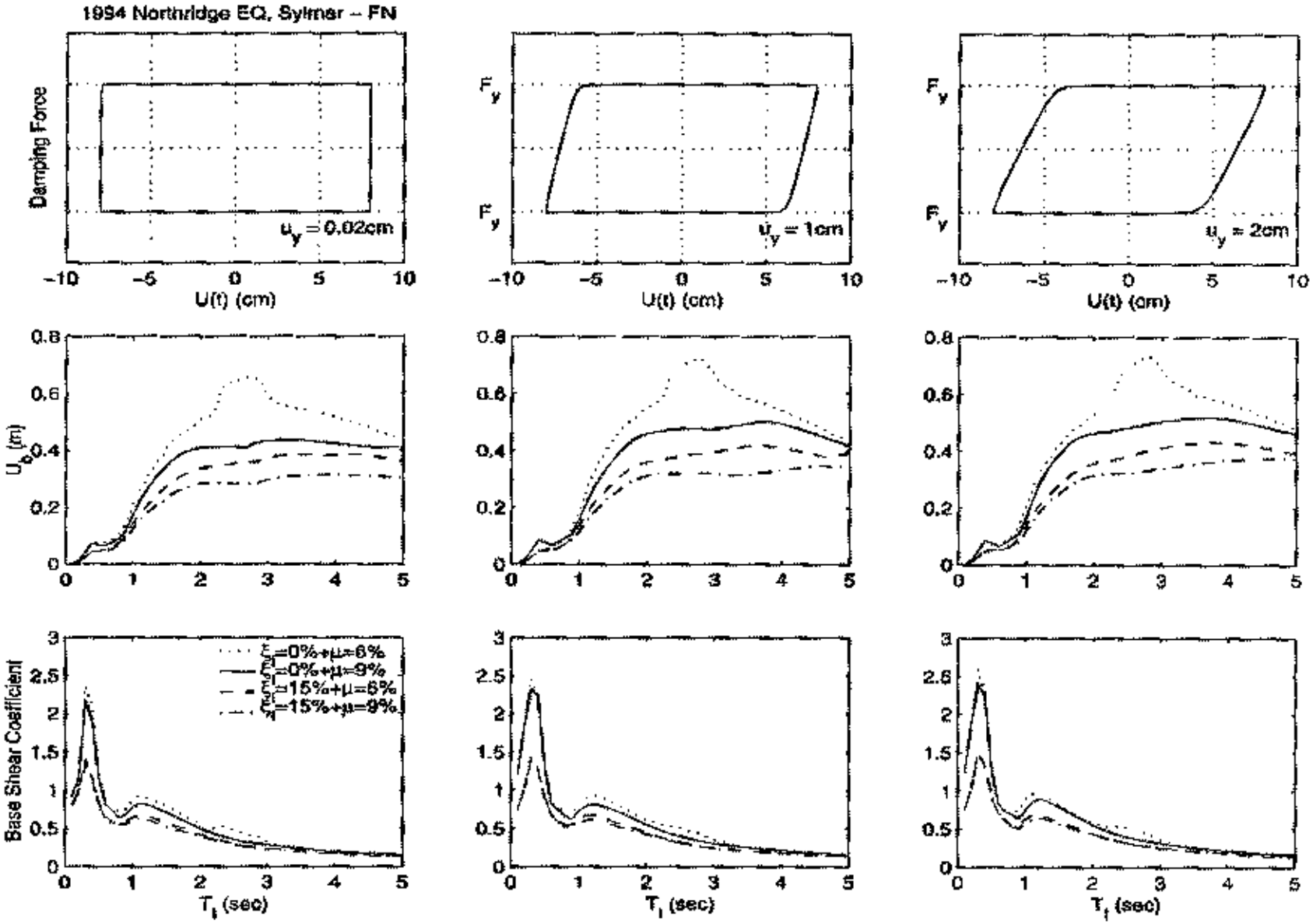

Figure 25: Displacement and base shear spectra of an isolated block subjected to the fault normal component of the Sylmar station record. Left: u_y = 0.2 mm; center: u_y = 10 mm; right: u_y = 20 mm.

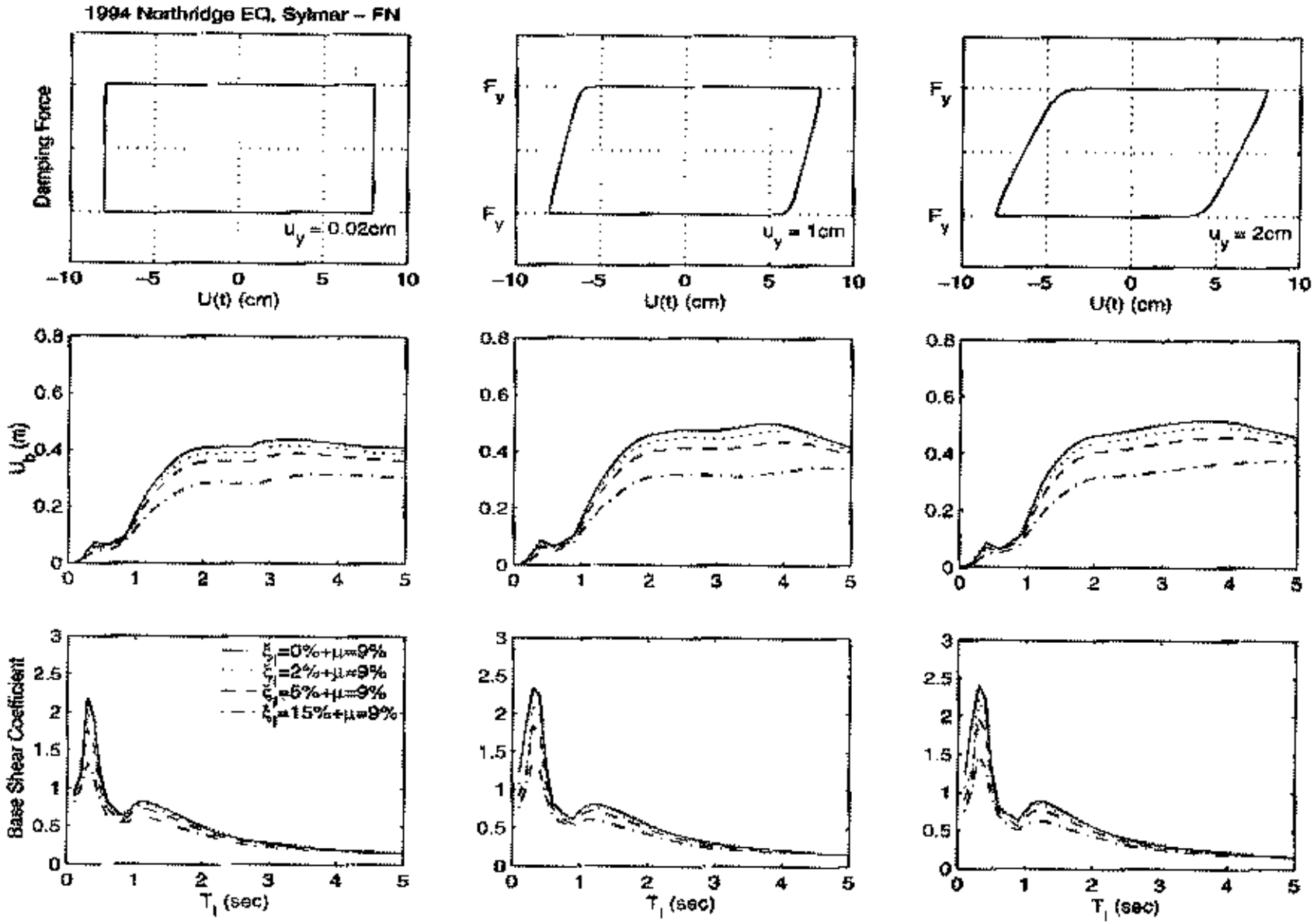

Figure 26: Displacement and base shear spectra of an isolated block subjected to the fault normal component of the Sylmar station record. Left: u_y = 0.2 mm; center: u_y = 10 mm; right: u_y = 20 mm.

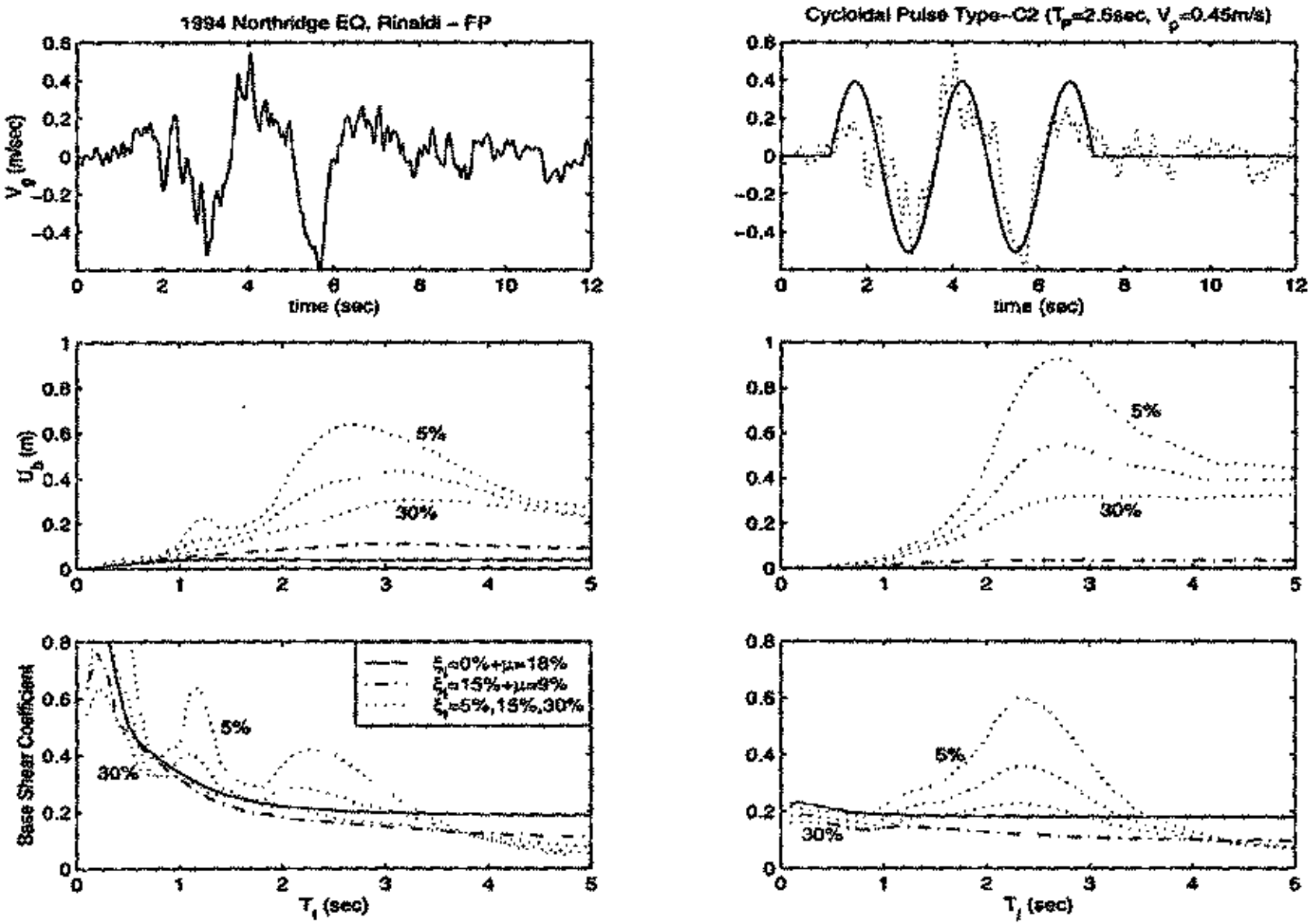

Figure 27: Displacement and base shear spectra of an isolated block subjected to the fault parallel component of the Rinaldi station record (left) and a type-C_2 pulse (right).

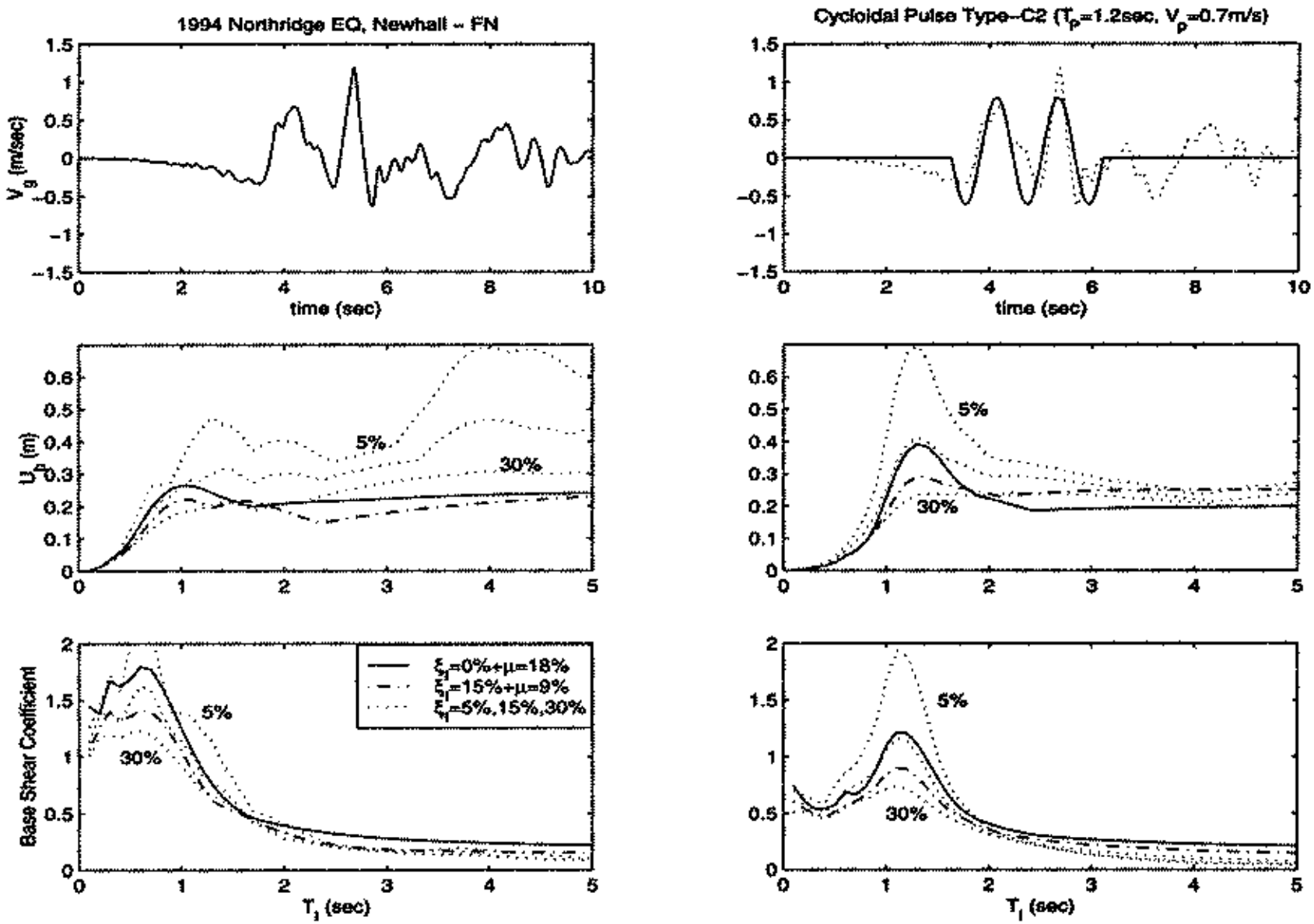

Figure 28: Displacement and base shear spectra of an isolated block subjected to the fault normal component of the Newhall station record (left) and a type-C_2 pulse (right).

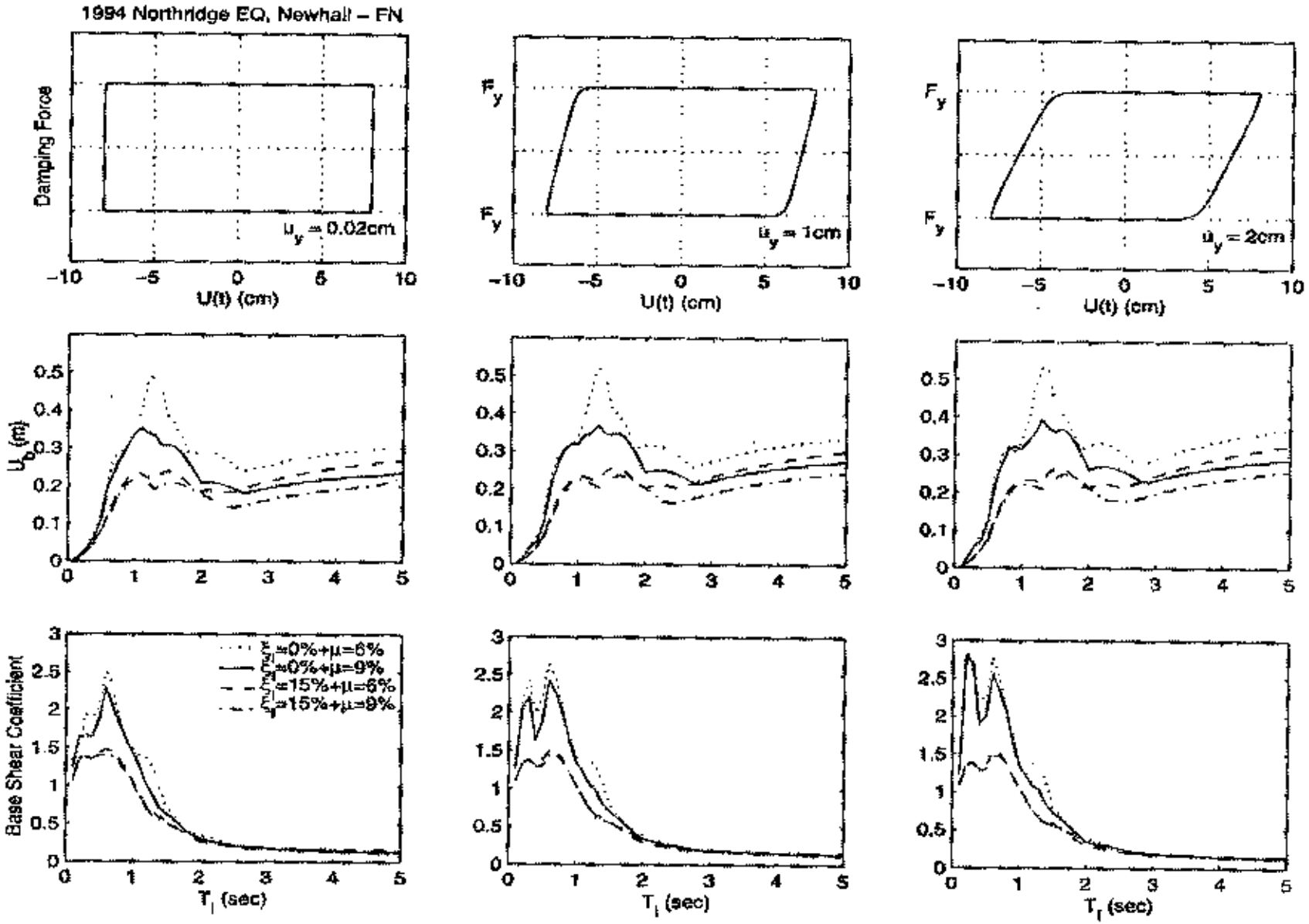

Figure 29: Displacement and base shear spectra of an isolated block subjected to the fault normal component of the Newhall station record. Left: $u_y = 0.2$ mm; center: $u_y = 10$ mm; right: $u_y = 20$ mm.

This parametric study on the response of 1-DOF systems indicates that, under near-source ground motion plastic dissipation forces of the order of 9% of the weight of the structure are very beneficial in reducing displacements without increasing base shears. Displacements can be further reduced with additional viscous damping. Furthermore, the ability to control the level of friction forces increases the effectiveness of the isolation system under certain motions. Accordingly, the findings of this study indicate the potential advantages that controllable fluid dampers have on seismic protection application.

We now investigate the effect of the viscous, viscoplastic and rigid-plastic dissipation mechanisms on the response of the 2-DOF structure shown in Figure 1 (bottom). As an example, Figure 30 plots the base displacement, base shear, superstructure drift and total acceleration time histories of the superstructure of a 2-DOF system equipped with the dissipation mechanisms introduced in the previous section. The isolation period is T_I = 2.0 sec, and the superstructure period is T_s = 0.25 sec. The response of the base of the 2-DOF structure when subjected to the Rinaldi station record is very close to the response of 1-DOF structure with the same isolation period (T_I = 2 sec) shown in Figure 13 (bottom). It is interesting to note that, by increasing the viscous damping from 15% to 30%, the base displacement decreased from 43.7 cm to 32.2 cm (30%), whereas the increase of interstory drift was less 1% and the increase in the superstructure acceleration was less than 2%, which shows that, in this case, additional damping substantially decreased the base displacement without affecting interstory drifts and superstructure accelerations. However, when friction damping is used (μ = 18%), the displacements are reduced only to 37.3 cm (16%), whereas interstory drift is increased by 45%, and superstructure acceleration is also increased by 45%. The combination of viscous (ξ_I = 15%) and hysteretic (μ = 9%) dissipation reduced base displacements to 34.6 cm (23% reduction), whereas interstory drift increased by 27% and superstructure acceleration increased by 30%.

The seismic performance of the 2-DOF isolated structure equipped with various types of damping mechanisms in its isolation system is summarized in Figure 31, where displacement, base shear, interstory drift and superstructure acceleration spectra are plotted for the fault normal component of the Rinaldi station record (left), a type-A pulse excitation with T_p^A = 0.8 sec (center) and a type-B pulse excitation with T_p^B = 1.3 sec (right). In this case, supplemental energy dissipation with viscous damping outperforms all other dissipation mechanisms. In contrast, Figure 32

shows that, under the Sylmar motion of the Northridge earthquake, an isolation system with T_I = 3 sec and a combination of viscous damping ξ_I = 15% and friction damping μ = 9% results in the most attractive response. Similar trends are observed in Figure 33, where an isolation system with T_I = 2.2 sec and a combination of viscous damping ξ_I = 15% and friction damping μ = 9% results in the most attractive response, since base displacements are substantially reduced without appreciably increasing base shear and superstructure accelerations.

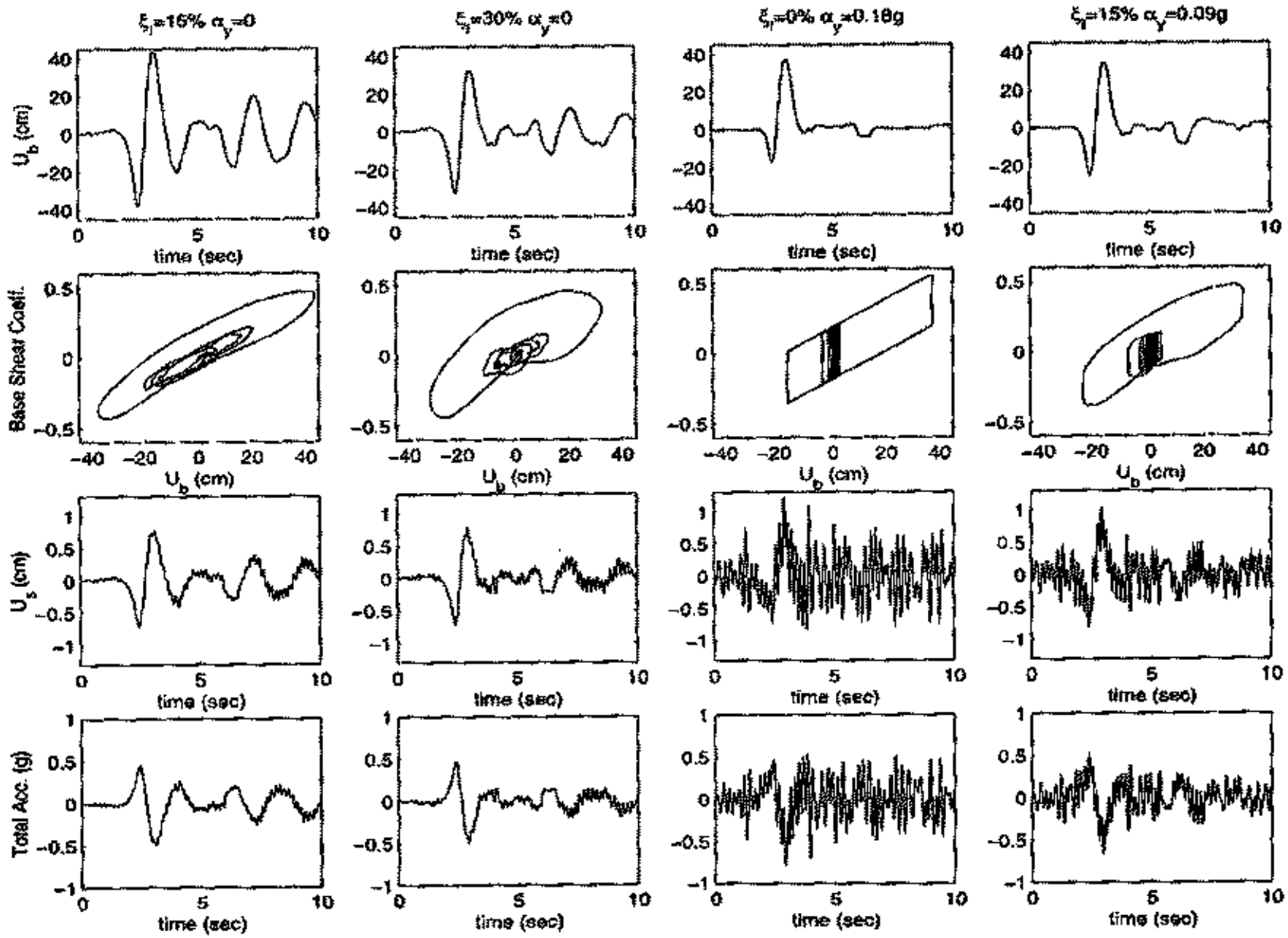

Figure 30: Response quantities of a 2-DOF isolated structure subjected to the fault normal component of the Rinaldi station record.

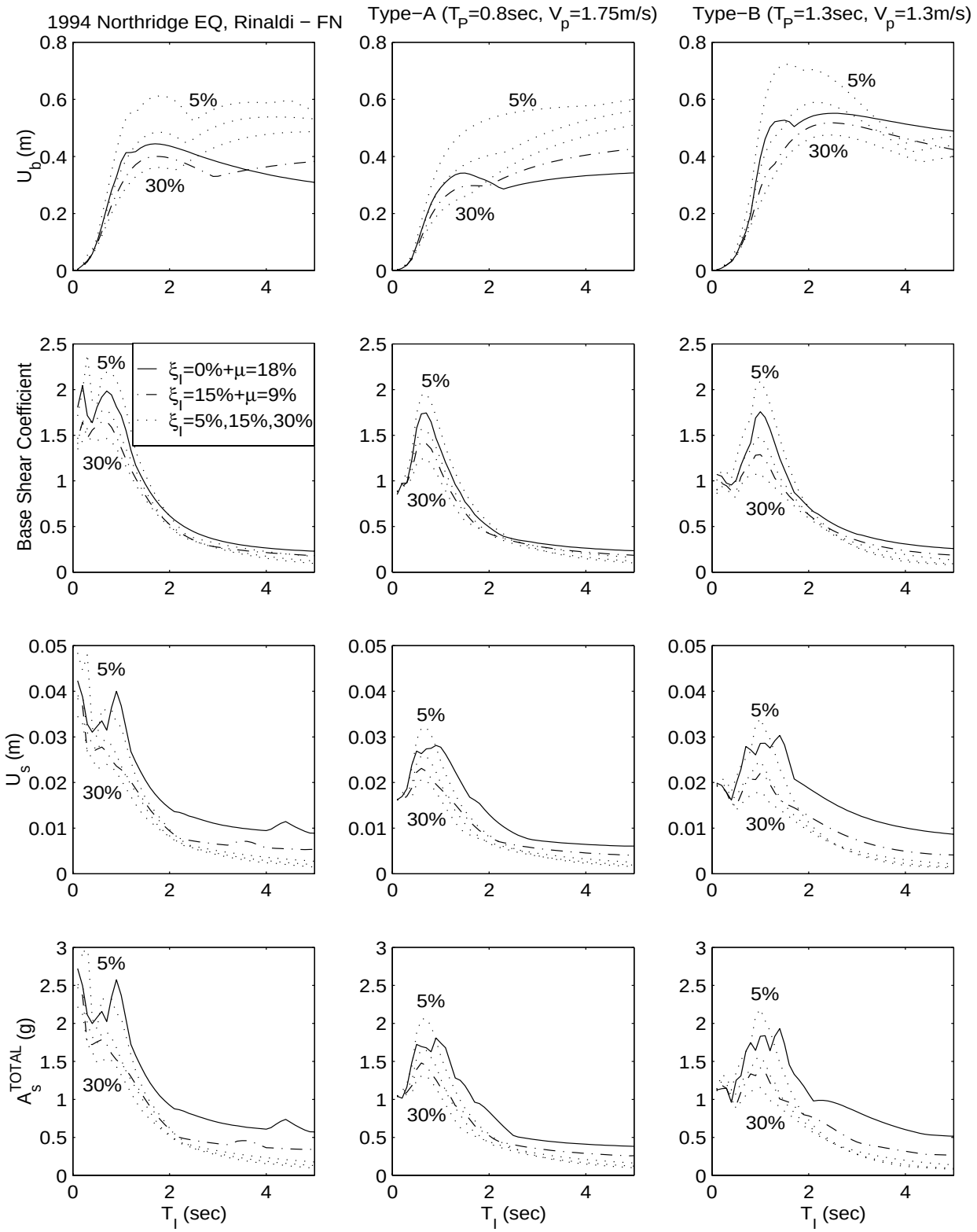

Figure 31: Base displacement, base shear, superstructure drift and total superstructure acceleration spectra of a 2-DOF isolated structure subjected to the fault normal component of the Rinaldi station record (left), a type-A pulse (center) and a type-B pulse (right).

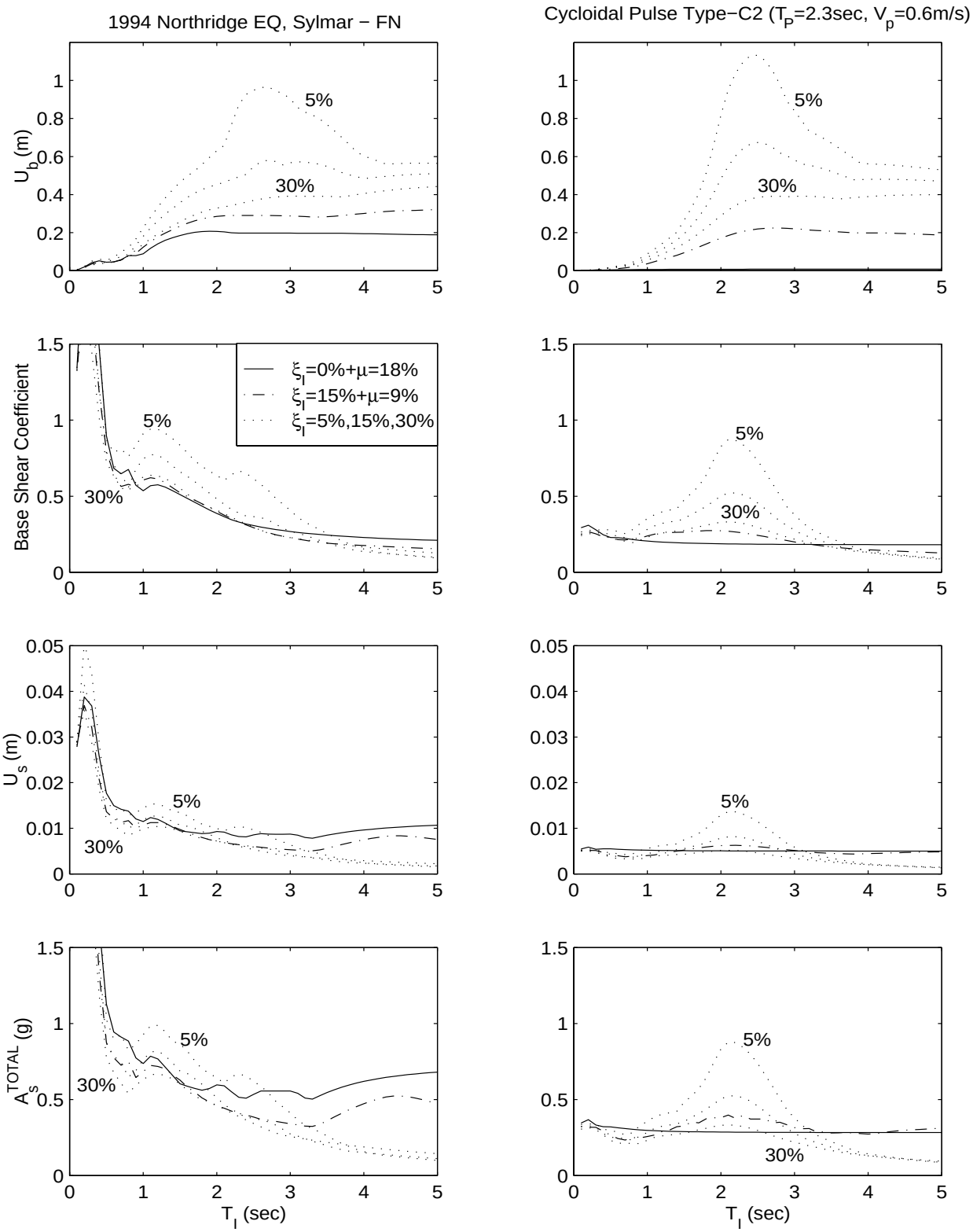

Figure 32: Base displacement, base shear, superstructure drift and total superstructure acceleration spectra of a 2-DOF isolated structure subjected to the fault normal component of the Sylmar station record (left) and a type-C_2 pulse (right).

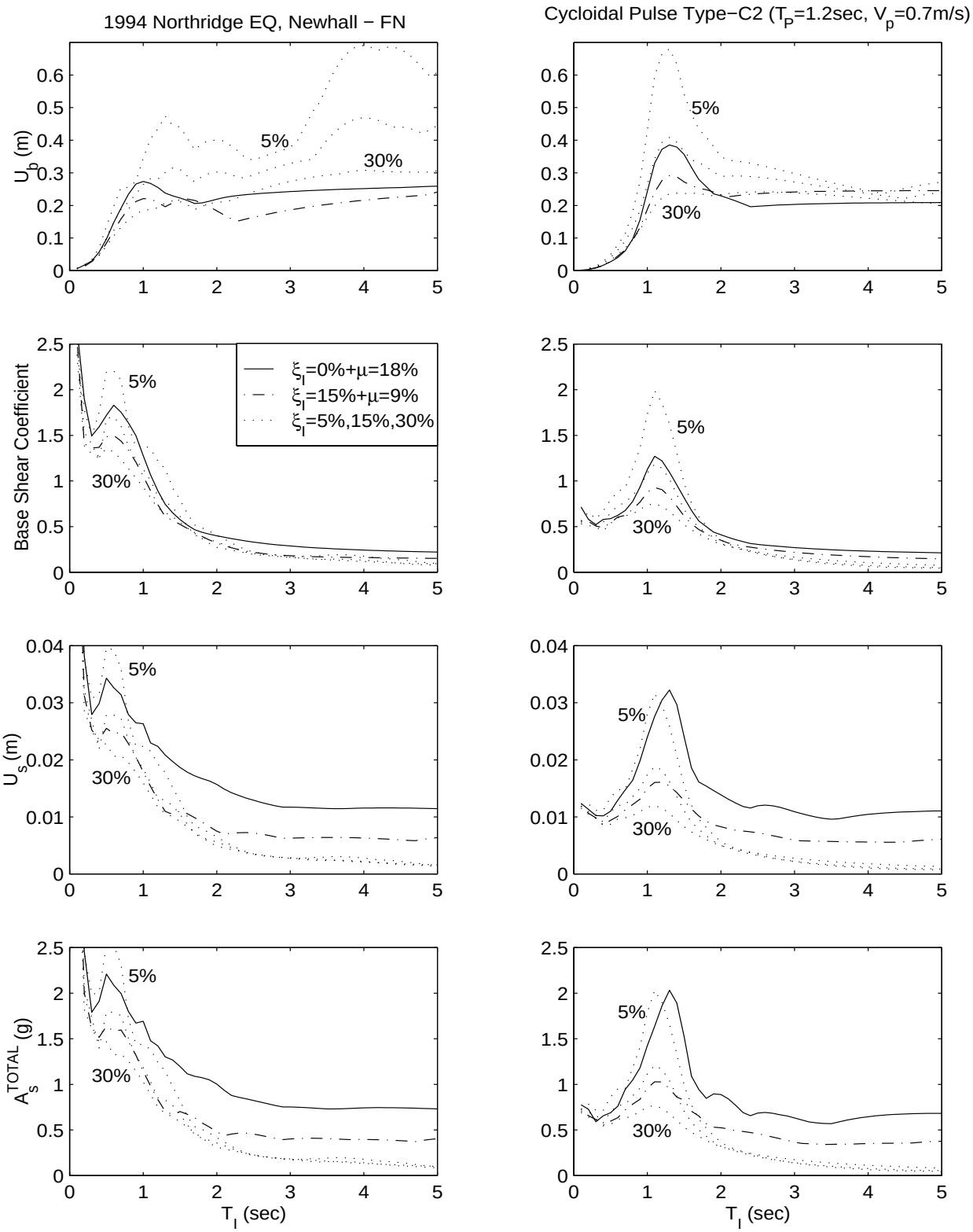

Figure 33: Base displacement, base shear, superstructure drift and total superstructure acceleration spectra of a 2-DOF isolated structure subjected to the fault normal component of the Newhall station record (left) and a type-C_2 pulse (right).

CHAPTER 6

CONCLUSIONS

The efficiency of various dissipative mechanisms to protect bridge structures from pulse-type and near-source ground motion has been investigated in detail. It was first shown that, under these motions, the concept of equivalent linear damping has limited meaning, since the transient response of a structure is more sensitive to the nature of the dissipation forces than to the amount of energy dissipated per cycle.

Physically realizable trigonometric pulses have been introduced, and their resemblance to selected near-source ground motions was illustrated. It is found that structural response quantities due to the recorded motions resemble the structural response quantities due to trigonometric pulse-type motions only when the isolation period reaches high values (i.e., T_I = 3.0 sec or more). The response of structures with relatively low isolation periods (i.e., T_I < 2.0 sec) is substantially affected by the high frequency that overrides the long-duration pulse. Therefore, the concept of seismic isolation is beneficial even for motions that contain long-velocity and displacement pulses. It is observed that a relatively low value of plastic (friction) damping (i.e., μ = 9%) removes any resonant effect that a long-duration pulse has on a long-period isolation system. According to this study, there is no need for extremely long isolation periods (i.e., T_I = 5.0) in order to go further away from the long period pulse that dominates a near-source ground motion. The study shows that the benefits of hysteretic dissipation are nearly indifferent to the level of the yield displacement and that they depend primarily on the level of the plastic (friction) force. Consequently, rigid-plastic behavior (sliding bearings) results to nearly the same response reduction as elastic-plastic behavior (lead rubber bearings) provided that both systems have the same yield (friction) force. The study concludes that, for isolated structures with isolation period $T_I \approx 3.0$ sec, a combination of viscous and friction dissipation forces is attractive, since displacements are substantially reduced without appreciably increasing base shears and superstructure accelerations. The study makes clear that under near-source ground motion, a time domain dynamic analysis is needed where the mechanical properties of isolation system are accounted for.

REFERENCES

1. Anderson, J. C. and Bertero, V. (1986). “Uncertainties in establishing design earthquakes,” *Journal of Struct. Eng.*, ASCE, Vol. 113, pp. 1709-1724.

2. Anderson, J. G., Bodin, P., Brune, J. N., Prince, J. and Singh, S. K. (1986). “Strong ground motion from the Michoagan, Mexico earthquake,” *Science*, Vol. 233, pp. 1043-1049.

3. ATC-17-1. (1993). *Proceedings of Seminar on Seismic Isolation, Passive Energy Dissipation, and Active Control*, Vol. 1&2, Applied Technology Council.

4. Campillo, M., Gariel, J. C., Aki, K. and Sanchez-Sesma, F. J. (1989). “Destructive strong ground motions in Mexico City: Source, path, and site effects during great 1985 Michoagan earthquake,” *Bulletin Seismological Soc. of America*, Vol. 79, No. 6, pp. 1718-1735.

5. Chopra, A. K. (1995). *Dynamics of Structures, Theory and Applications to Earthquake Engineering*, Prentice Hall, New Jersey.

6. Clough, R. W. and Penzien, J. (1993). *Dynamics of Structures*, McGraw-Hill, New York.

7. Hall, J. F., Heaton, T. H., Halling, M. W. and Wald, D. J. (1995). “Near-source ground motions and its effects on flexible buildings,” *Earthquake Spectra* Vol. 11, pp. 569-605.

8. Iwan, W. D. (1997). “Drift spectrum: measure of demand for earthquake ground motions,” *Journal of Structural Engineering*, Vol. 123, No. 4, pp. 397-404.

9. Iwan, W. D. and Chen, X. D. (1994). “Important near-field ground motion data from the Landers earthquake,’ *Proc. 10th European Conf. Earthquake Engrg.*, Vienna.

10. Jacobsen, L. S. and Ayre, R. S. (1958). *Engineering Vibrations*, McGraw-Hill, New York, NY.

11. Kelly, J. M. (1997). *Earthquake Resistant Design with Rubber*, Springer-Verlag, London.

12. Kramer, S. L. (1996). *Geotechnical Earthquake Engineering*, Prentice Hall, New Jersey.

13. Makris, N. (1997). “Rigidity-plasticity-viscosity: can electrorheological dampers protect base-isolated structures from near-source ground motions?” *Earthquake Engineering and Structural Dynamics*, Vol. 26, pp. 571-591.

14. Makris, N. and Constantinou, M. C. (1991). “Analysis of motion resisted by friction: I. Constant-Coulomb and linear-Coulomb friction,” *Mech. Struct. & Mach.*, Vol. 19, No. 4, pp. 477-500.

15. Mokha, A., Constantinou, M. C. and Longhorn, A. M. (1988). “Teflon bearings in aseismic base isolation: Experimental studies and mathematical modeling,” *Technical Report NCEER-88-0038,* SUNY Buffalo.

16. Shames, I. H. and Cozzarelli, F. A. (1992). *Elastic and Inelastic Stress Analysis,* Prentice Hall, New Jersey.

17. *Uniform Building Code,* (1994). International Conference of Building Officials, Whittier, CA.

18. Wen, Y. K. (1975). “Approximate method for nonlinear random vibration,” *Journal of the Engineering Mechanics Division,* ASCE, Vol. 101, EM4, pp. 389-401.

19. Wen, Y. K. (1976). “Method for random vibration of hysteretic systems,” *Journal of the Engineering Mechanics Division,* ASCE, Vol. 102, EM2, pp. 249-263.